Subproject C3.12

Nanoscale Luminescent Materials for Blue Light Excitation

Principle Investigators: Claus Feldmann

CFN-Financed Scientists: Dr. Marcus Roming (1/2 E13, 17 months), Fabian Gyger (1/2 E13, 24 months)

Further Scientists: Marit May

Institut für Anorganische Chemie
Karlsruhe Institute of Technology (KIT)

Nanoscale Luminescent Materials for Blue Light Excitation

Introduction and Summary

Nanoscale luminescent materials are of increasing importance concerning established technologies (e.g. displays, lighting, X-ray detection). Aiming at up-coming applications, nanoscale phosphors are essential. This includes transparent luminescent layers or markers (e.g. on metal, ceramics, plastics, paper), luminescent fillers in transparent matrices (e.g. glass, plastics) as well as bio-medical applications, such as FRET-assays, bio-labelling, optical imaging or photo-therapy.

II-VI or III-V semiconductor-type quantum-dots as well as rare-earth doped metal phosphates represent todays state-of-the-art materials with quantum yields exceeding 50 %. Especially, core-shell structures turned out to be most successful. To realize top-quality luminescent nanocrystals, on the one hand, synthesis has to be performed at elevated temperatures (typically 150-250°C) in order to minimize lattice defects. On the other hand, coordinating solvents or stabilisers (e.g., trioctylphosphine, octylphosphate, octylamine, thioglycerol, diethylene glycol, oleic acid, polyvinyl pyrrolidone) are essential to steer the particle size, to control the degree of agglomeration, and to protect the particles surface. A modification of the resulting 'synthesis-determined' surface conditioning requires additional process steps and bears the risks of colloidal collapse, agglomeration and surface damage. In summary, the synthesis is often complicated and time-consuming. Toxic solids, solvents or stabilisers are frequently included. All these issues can be major limitations aiming at technical application.

With this CFN-subproject we have developed a novel and facile synthesis of highly luminescent nanomaterials based on ionic liquids (ILs) as reaction media. ILs in recent years have attracted considerable interest due to their exceptional features, such as a wide liquid range, thermal stability, non-coordinating properties, electrochemical stability and adjustable solvent polarity. In between, ILs have significant impact, especially, on organic synthesis. On the contrary, an exploration of their benefits towards a synthesis of nanocrystals has just been started. In sum, we could gain high-quality nanomaterials such as $LaPO_4$:Ce,Tb, YVO_4:Eu@YF_3, CaF_2:Ce,Tb, Zn_2SiO_4:Mn, $BiPO_4$:Tb, $In_2(MoO_4)_3$:Eu and $CaWO_4$ via the novel ionic-liquid-based approach.

In addition to metal-doped luminescent materials, organic inorganic hybrids such as the compound ZrO(FMN) were introduced as novel luminescent materials. ZrO(FMN) has several important features, including a quick and easy water-based synthesis, potentially low costs of production, a high biocompatibility, and a variable concentration of the incorporated dye, allowing for quasi-infinite number of luminescent centers. Typical key issues for quantum dots as well as metal-doped nanoparticles, such as high-temperature crystallization and core-shell type surface conditioning, do not need any consideration. Taking all these aspects together, ZrO(FMN) might be a promising alternative to existing luminescent nanomaterials. Its use as a luminescent biomarker and its biocompatibility has been successfully tested as a proof of the concept in living mice and cells. Finally, the concept of DMZP's has already been extended to red and blue emission as well as to luminescent switching.

Nanoscale luminescent materials as prepared in this CFN-subproject were transferred to several cooperation partners, including optical imaging for medical applications (Dr. K. Dittmar, Helmholtz-Zentrum für Infektionsforschung, Braunschweig), incorporation in polymers (Prof. C. Barner-Kowollik, KIT), incorporation in metal-organic frameworks (Prof. K. Müller-Buschbaum, Universität Würzburg, Prof. P. Behrends, Universität Hannover), characterization via solid state NMR (Dr. J. Schmedt a.d.G., LMU München).

In the timeframe 2008-2010, subproject C3.12 has led to 16 publications, among which is 1 review article in *Angew. Chem.*, 1 in *Angew. Chem.*, 1 in *Chem. Commun.*, 1 in *Chem. Mater.* and 1 patent.

1. Metal-doped nanoscale luminescent materials

Nanoscale luminescent materials are of increasing importance concerning established technologies (e.g. displays, lighting, X-ray detection).[1] Aiming at up-coming applications, nanoscale phosphors are essential. This includes transparent luminescent layers or markers (e.g. on metal, ceramics, plastics, paper), luminescent fillers in transparent matrices (e.g. glass, plastics) as well as bio-medical applications, such as FRET-assays, bio-labelling, optical imaging or photo-therapy.[2]

II-VI or III-V semiconductor-type quantum-dots as well as rare-earth doped metal phosphates represent todays state-of-the-art materials with quantum yields exceeding 50 %.[3] Especially, core-shell structures turned out to be most successful.[4] To realize top-quality luminescent nanocrystals, on the one hand, synthesis has to be performed at elevated temperatures (typically 150-250°C) in order to minimize lattice defects. On the other hand, coordinating solvents or stabilisers (e.g., trioctylphosphine, octylphosphate, octylamine, thioglycerol, diethylene glycol, oleic acid, polyvinyl pyrrolidone) are essential to steer the particle size, to control the degree of agglomeration, and to protect the particles surface. A modification of the resulting 'synthesis-determined' surface conditioning requires additional process steps and bears the risks of colloidal collapse, agglomeration and surface damage. In summary, the synthesis is often complicated and time-consuming. Toxic solids, solvents or stabilisers are frequently included. All these issues can be major limitations aiming at technical application.

Via a novel and facile synthesis highly luminescent $LaPO_4$:Ce,Tb nanocrystals can be alternatively prepared based on ionic liquids (ILs) as reaction media. ILs in recent years have attracted considerable interest due to their exceptional features, such as wide liquidus range, thermal stability, non-coordinating properties, electrochemical stability and adjustable solvent polarity.[5] In between, ILs have significant impact, especially, on organic synthesis.[6] On the contrary, an exploration of their benefits towards a synthesis of nanocrystals has just been started.[7] Due to the non-coordinating properties of ILs,[5,8] a complete removal after the synthesis, in principal, should be much easier compared to standard coordinating solvents. In contrast, surface stabilisation at elevated temperatures, which is prerequisite to non-agglomerated and highly luminescent nanoscale phosphors, will be significantly reduced. In order to avoid agglomeration, our strategy is a fast and short-timed heating. Due to the high polarity of ILs, this can be performed by microwave irradiation.

In a first step of the synthesis, a solution of the rare earth chlorides in tributylmethylammonium triflylimide and a co-solvent (e.g., EtOH, DMF, DMSO, pyridine) was added at 70°C to the phosphate precursor (e.g., H_3PO_4, ammonium or pyridinium phosphate), again dissolved in IL and co-solvent. The ionic liquid was selected from a variety of candidates due to its extraordinary thermal and chemical stability.[9] Precipitation of $LaPO_4$:Ce,Tb occurs immediately, indicated by a slight opalescence. Thereafter, all volatiles were removed under reduced pressure. In a second step, the crystallinity of the preformed nanoparticles was enhanced by heating the dispersion in a microwave oven within about 10 s to 300°C. Subsequent to centrifugation and suited washing, the nanocrystals were collected with yields of 90 %. The obtained white powder can be easily redispersed in ethanol by sonification. While exciting with UV-light, the resulting transparent dispersions show intense green emission (Fig. 1).

Size and morphology of the $LaPO_4$:Ce,Tb nanocrystals were examined by electron microscopy. TEM micrographs show spherical to slightly ellipsoidal particles, 9-12 nm in size (Fig. 2A). High resolution images exhibit lattice fringes, indicating the crystallinity of the particles (Fig. 2B). TEM/SEM micrographs of samples, prepared from ethanolic dispersions, display a multitude of almost spherical and monodispersed particles. Here, a particle diameter of 10(1) nm is calculated by statistical evaluation of 170 particles (Fig. 2C, Fig. 2D). Electron diffraction as well as X-ray

powder diffraction patterns evidence the monoclinic monazite type of structure of the nanocrystalline material (Fig. 2B).[10] With the assumption of spherical particles, the mean particle diameter can be deduced based on *Scherrer's* equation to values of 8 to 10 nm, which is in accordance with electron microscopy.

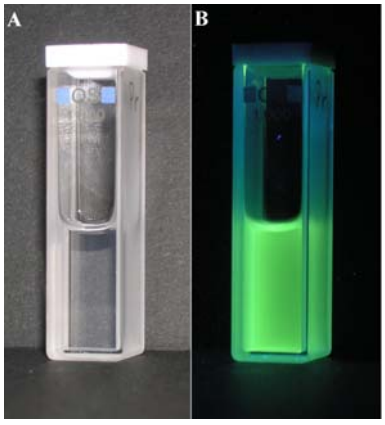

Figure 1. Transparent dispersion of $LaPO_4$:Ce,Tb nanocrystals redispersed in ethanol: in day-light (A) and with UV-excitation (B).

To verify particle diameter and size distribution in suspension, dynamic light scattering was performed. Firstly, as-prepared $LaPO_4$:Ce,Tb is investigated after washing and redispersing in ethanol. Taking a slight missmatch between the viscosity of pure solvent and real dispersion into account, with 18 nm the measured hydrodynamic diameter corresponds well to the results from electron microscopy. While comparing infrared spectra of the pure IL with as-prepared and washed $LaPO_4$:Ce,Tb powders, the surface conditioning of the particles can be verified. In addition to vibrational bands related to phosphate (1100-900, 650-500 cm^{-1}) and water (3500-3300, 1630 cm^{-1}), the constituents of the IL are indicated by weak absorption bands (ν(C-H) = 2970-2880 cm^{-1}; ν(S-O) = 1470-1060 cm^{-1}).[11] As a result, effective prevention of particle agglomeration has to be attributed to charge stabilisation.

The IL can be removed completely upon addition of dilute NaCl-solution to an ethanolic dispersion of LaPO:Ce,Tb. With this treatment, IR-spectra of powder samples do indeed not show any vibrational bands of the IL constituents. After NaCl-treatment and centrifugation, redispersion of $LaPO_4$:Ce,Tb is still possible, for instance, in ethanol by prolonged sonification. With 21 nm the average diameter is almost identical to as-prepared dispersions, excluding significant agglomeration. This is even more remarkable, since coordinating solvents and modifiers are absent. Moreover, straight forward removal of the IL optionally enables to realize of a surface conditioning, which is adjusted to the specific needs of a certain application, independent from the conditions of synthesis.

The luminescence of $LaPO_4$:Ce,Tb is well established for bulk as well as for nanoscale materials.[3,12] Prior to energy transfer from Ce^{3+} to Tb^{3+}, UV-excitation on Ce^{3+} via $4f^1 \rightarrow 4f^05d^1$ transition occurs. This is followed by Tb^{3+} emission of green light due to $^5D_4 \rightarrow {}^7F_J$ relaxation. Emission spectra of as-prepared $LaPO_4$:Ce,Tb (45 mol-%, 15 mol%) dispersed in ethanol correspond to the expectation. The quantum yield was measured to 0.70(2) considerung Tb^{3+} emission only, and to 0.90(2) taking the emission of Ce^{3+} into account. These values are even more interesting since neither an inorganic shell nor coordinating surface modifiers are required to protect the nanocrystals. In fact, the quantum yield is close to the bulk material (0.86 for Tb-emission, 0.93 for sum of Ce/Tb-emission).[13]

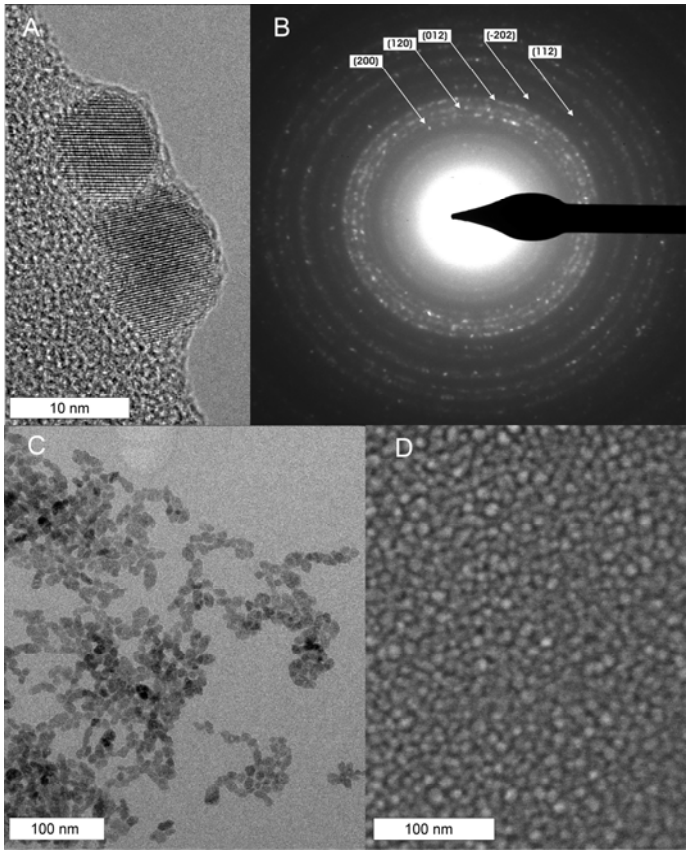

Figure 2. TEM/SEM images of as-prepared $LaPO_4$:Ce,Tb: A) HR-TEM micrograph showing lattice fringes; B) Electron diffraction pattern of a bundle of particles including *Miller* indices; C) TEM and D) SEM micrograph indicating the uniformity of particles.

Luminescent thin films

Previous studies have already shown the IL constituents to be adhered on the surface of the nanocrystals via charge interaction. Due to the 'non'-coordinating properties of the IL, its constituents can be removed completely just by washing with ethanol that is saturated with NaCl. Considering this finding, other types of specific surface modification should also be possible. To this concern, phase transfer of elemental metals driven by amines such as oleylamine or 4-4-dimethylaminopyridine (DMAP) is well known.[17] It turned out that such a phase transfer works also very well in case of as-prepared $LaPO_4$:Ce,Tb. After addition of oleylamine, by stirring the nanocrystals can be transferred from a polar, hydrophilic phase (e.g. methanol, ethanol, diethylene glycol) to a non-polar, hydrophobic dispersant (e.g. hexane, toluene) (Fig. 3). Such a phase transfer for application-oriented issues is important in order to embed or to attach luminescent nanocrystals in or on non-polar substrates (e.g. plastics).

Nanoscale luminescent materials are highly requested for embedding in transparent matrices (e.g. glass, plastics) or to realize transparent luminescent layers (e.g. on glass, plastics, metal, paper) for labeling, signaling and design purposes.[18] To this concern, ink-jet printing of dispersions containing as-prepared $LaPO_4$:Ce,Tb on standard overhead transparencies is studied as a proof of concept (Fig. 4). Due to the ink-jet equipment applied here, dispersions in ethanol were limited to solid contents of 2 wt-% for reasons of nozzle clogging. In order to still establish a certain layer thickness (about 30 nm), printing was repeated as a layer-by-layer process several times. Black letters on paper, which are positioned behind the overhead transparency, qualitatively confirm its transmittance to be almost unaffected after printing. The printed structure is only barely visible in daylight (Fig. 4A), but can clearly be recognized under UV-excitation (Fig. 4B). Due to commercial overhead transparencies containing optical bleachers, blue emission is observed in addition.

Additive color mixing altogether results in a greenish white appearance of the printed structure. Since aspects such as viscosity, solids content and composition of the ink, adhesion, haze and definition of the layer as well as the printing equipment itself have not been optimized so far; a substantial increase in layer quality can be expected based on professional printing.

As a second example of potential technical application, a full transparent dielectric barrier discharge (DBD) lamp is aimed. DBD lamps, in general, are relevant for general lighting as an alternative to standard fluorescent lamps (FL). This is especially for environmental issues, namely to substitute the mercury discharge used in FL lamps by a xenon discharge.[19] Driven by a pulsed voltage, the latter is applied in DBD lamps and leads to a Xe-excimer emission, exhibiting its highest intensity at 173 nm. This vacuum ultraviolet (VUV) emission is converted to visible light by a phosphor layer, which is located on the inside of the glass bulb. Figure 4A schematically shows the construction of such a DBD lamp. As a state-of-the-art, the phosphor layer consists of micron sized phosphor particles (5 to 8 µm in diameter). Due to the scattering of this layer the lamp for physical reasons can not be transparent. While introducing nanoscale $LaPO_4$:Ce,Tb as a phosphor layer, however, all scattering in the visible can be excluded (Fig. 5B). Subsequent to evacuation, careful removal of all moisture, filling with xenon and connecting to two grid electrodes, the Xe-discharge can be turned on. Indeed, green emission of $LaPO_4$:Ce,Tb is observed (Fig. 5C). With this prototype a first full transparent DBD lamp containing nanoscale luminescent materials is shown.[20] In principle, such a device can be interesting as a kind of a 'luminescent window', which has to be transparent throughout the day, but which can be illuminated during the night by means of labelling, signalling or advertising. Subsequent to optimizing, for instance, the thickness of the phosphor layer and after exchanging the metal grid by ITO (indium tin oxide) electrodes, also extended transparent flat light sources might be within reach.

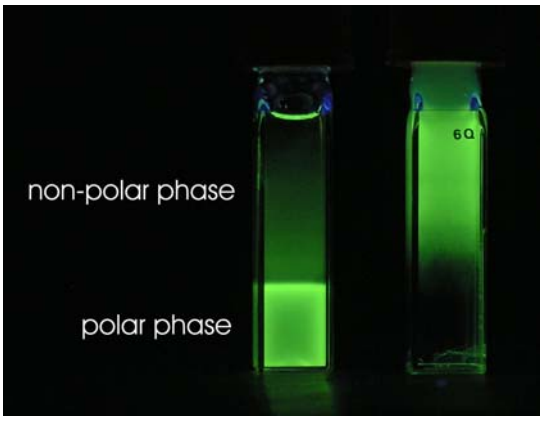

Figure 3: Oleylamine-driven phase transfer of nanocrystalline $LaPO_4$:Ce,Tb from the polar phase (A, e.g. methanol, ethanol, diethylene glycol) to a non-polar dispersant (B, e.g. hexane, toluene)

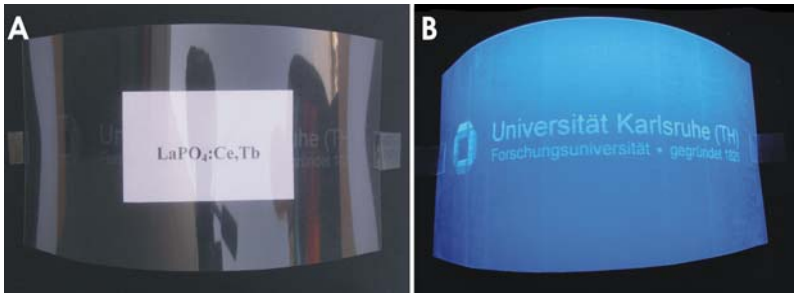

Figure 4. Picture with ink-jet printed $LaPO_4$:Ce,Tb on overhead transparency: in daylight (A) and under UV-excitation (B, $\lambda_{excitation}$ = 254 nm)

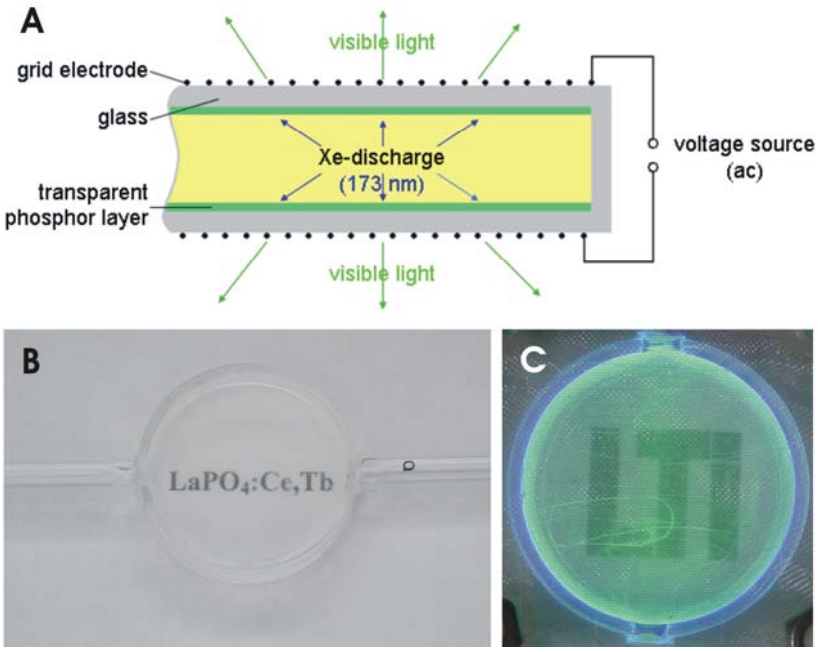

Figure 5. Scheme (A) and photos of dielectric barrier discharge (DBD) lamp subsequent to $LaPO_4$:Ce,Tb layer deposition (B) and under conditions of Xe-discharge (C)

Zn_2SiO_4:Mn

Ionic liquids containing metal cations have gained some interest combining a joint function as a solvent and a catalyst. As an example, zinc containing ionic liquids (Zn-IL) have been identified to catalyze Diels-Alder reactions or acetylation reactions.[21-23] In contrast, the usage of ionic liquids as an entire reactant in chemical synthesis is quite rare till now.[24] Aiming at luminescent nanomaterials we could also use such a strategy. We use ionic liquids for both - as a solvent as well as a reactant. Practically, Zn_2SiO_4:Mn was synthesized applying the ionic liquid $[N(Me)(Bu)_3][N(Tf)_2]$ (IL) as a solvent and the zinc-containing ionic liquid $[MeBu_3N][ZnCl_3/Zn_2Cl_5]$ (Zn-IL) as a reactant. Additional starting materials are $Si(OC_2H_5)_4$ and $MnCl_2$. Subsequent to the formation of an homogeneous solution, nucleation is initiated by addition of $[Me_4N](OH)$. For optimal conditions of nucleation this step is performed at slightly elevated temperatures (70 °C). To support a controlled particle growth and to remove all volatiles (e.g. water, ethanol), the suspension, thereafter is firstly evacuated and secondly heated to 250 °C. Furthermore, very fast heating via microwave irradiation is performed and led to optimal results with respect to the uniformity of the particles in size and morphology as well as with regard to the absence of agglomerates.

Subsequent to synthesis, particle separation and washing, as-prepared Zn_2SiO_4:Mn is yielded as a light brown powder. The color is ascribed to a low amount of Mn^{4+} due to a partial oxidation of Mn^{2+}. This finding is well-documented and has been often observed for bulk Zn_2SiO_4:Mn, too.[25] After resuspension in diethylene glycol (DEG) the particles are colloidally stable within weeks. Particle size and the size distribution of as-prepared Zn_2SiO_4:Mn are determined by DLS as well as by SEM (Fig. 6). Considering that hydrodynamic diameters are gained from DLS analysis, the resulting average values of 33 nm (DLS) and 32 nm (SEM) are in good aggreement and evidence the absence of agglomerates. X-ray diffraction patterns indicate as-prepared Zn_2SiO_4:Mn to be non-crystalline. At first glance, this finding is rather unexpected since highly crystalline compounds can often be realized based on the high-boiling points as a special feature of the ionic liquid. On the other hand, crystallization of bulk Zn_2SiO_4:Mn is also observed at temperatures of 800 to 1200 °C.

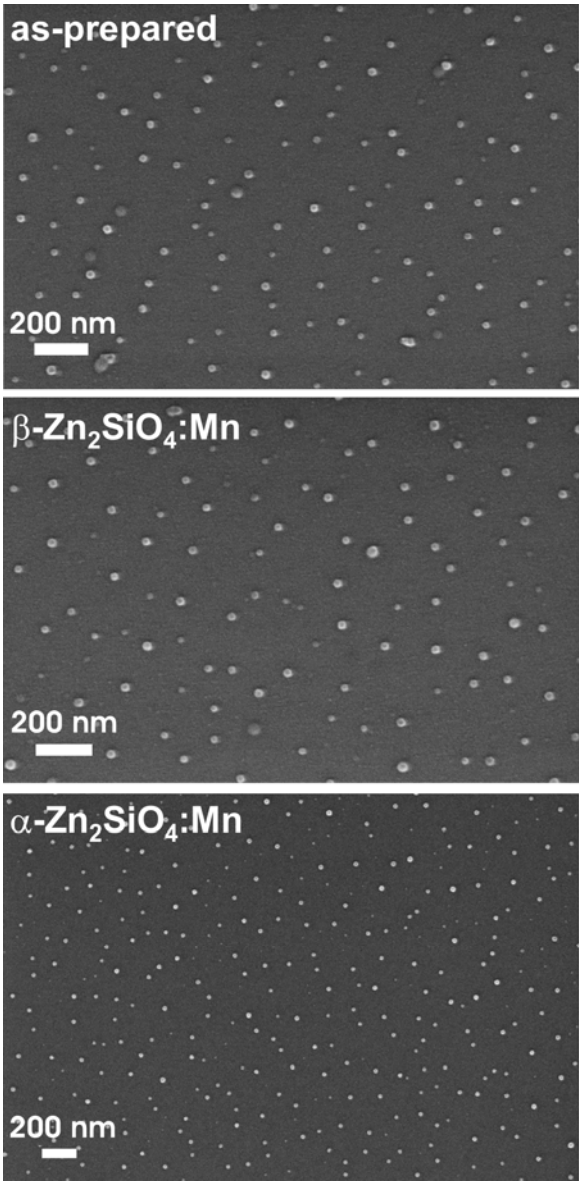

Figure 6: SEM images showing size and size distribution of as-prepared non-crystalline Zn_2SiO_4:Mn, as well as annealed β-Zn_2SiO_4:Mn (15 min, 750 °C) and α-Zn_2SiO_4:Mn (15 min, 1000°C).

Since as-prepared Zn_2SiO_4:Mn is non-crystalline, additional measures are applied to determine its chemical composition. To this concern, infrared spectroscopy is invoked. The characteristic strong vibrational bands can be related to the $[SiO_4]^{4-}$ tetrahedron and correspond to reference spectra of willemite: $\nu(SiO_4)$ = 1100-900 cm^{-1}, $\delta(SiO_4)$ = 600-400 cm^{-1}. Moreover, a strong OH-related band is observed (ν(OH): 3600-3000 cm^{-1}), which can be attributed to Si-OH groups. Based on previous investigations, additional weak bands can be related to the ionic liquid (ν(CH): 2980-2880 cm^{-1}, δ(CH): 1500-1200 cm^{-1}, ν(SO) = 1200-1100 cm^{-1}) and H_2O ($\delta(OH_2)$: 1650-1620 cm^{-1}) adhered to the particle surfaces. To validate a potential crystallization of as-prepared Zn_2SiO_4:Mn thermal analysis is carried out. According to thermogravimetry (TG) a continuous weight loss of about 20 wt-% is observed between 100 °C and 600 °C. This weight loss can be mainly attributed to water stemming from condensation reactions when establishing the silicate network. In addition, evaporation or decomposition of adhered water and ionic liquid constituents might occur. An exothermic DTA signal at 590 °C, furthermore, hints to a crystallization the powder sample.

The results of thermal analysis are confirmed by infrared spectra of Zn_2SiO_4:Mn samples, which have been annealed for 15 min at 750 °C. Vibrations related to IF and water are vanished. Sharpening and splitting of $[SiO_4]^{4-}$-related vibrations indicate the tetrahedral building unit now with a reduced site symmetry inside the crystalline lattice. XRD patterns of Zn_2SiO_4:Mn annealed for 15 min at 750 °C clearly evidence the prescence of β-Zn_2SiO_4 as a crystalline phase, which contains only minor amounts of α-Zn_2SiO_4. This yellow emitting modification is described with tetrahedral as well as octahedral coordination of Zn^{2+}. Note that a detailed crystal structure determination of β-Zn_2SiO_4 is still lacking. The thermodynamically more stable rhomboedric α-Zn_2SiO_4 exhibits zinc sites with tetrahedral coordination only. This green emitting modification is obtained when annealing as-prepared Zn_2SiO_4:Mn for 15 min at 1000 °C.

With annealing and crystallization at temperatures above 600 °C, and in view of the underlying huge surfaces of the nanoscale particles, a more or less complete aggregation is to be expected and has been observed most often. Surprisingly, resuspension of β-Zn_2SiO_4 and even of α-Zn_2SiO_4 is possible just applying ultrasonification. DLS analysis as well as SEM images confirm the nanocrystals treated at 750 and 1000 °C still to be nanoscaled, non-agglomerated and redispersible (Fig. 6). Average particle diameters of β-Zn_2SiO_4 are found with 19 nm (DLS) and 18 nm (SEM). In the case of of α-Zn_2SiO_4 values of 15 nm (DLS) and 14 nm (SEM) are measured. While comparing these results with as-prepared non-crystalline Zn_2SiO_4:Mn a significant shrinkage in diameter (40 % up to 55 %) is observed. This effect - which is in accordance with an increasing materials density during crystallization - may efficiently limit the interparticular contacts and therefore reduce agglomeration. Altogether, the absence of agglomerates even after annealing can be attributed to three items: 1. the thermal processing in general, namely a short-timed annealing (15 min); 2. a stabilizing layer of IL constitutents up to temperatures of 500 °C; 3. a significant volume shrinkage of about 40 % (β-Zn_2SiO_4) and 55 % (α-Zn_2SiO_4).

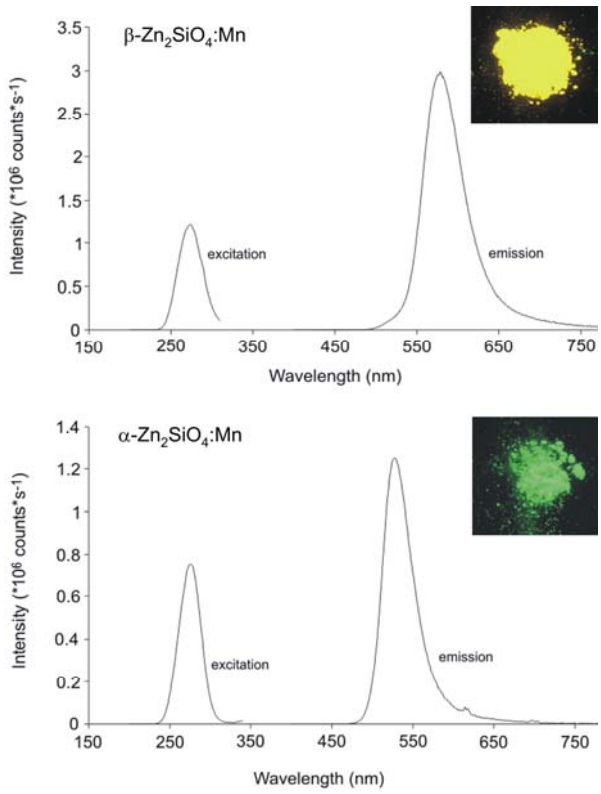

Figure 7: Excitation and emission spectra of β-Zn_2SiO_4:Mn ($\lambda_{emission}$ = 579 nm, $\lambda_{excitation}$ = 254 nm) and α-Zn_2SiO_4:Mn ($\lambda_{emission}$ = 529 nm, $\lambda_{excitation}$ = 254 nm) as well as photos displaying the emission of powder samples ($\lambda_{excitation}$ = 254 nm).

The luminescent properties of Zn_2SiO_4:Mn are well-known for bulk samples.[26] Luminescence of nanoscaled Zn_2SiO_4:Mn can be expected to be very similar. Excitation and emission spectra of nanoscale β-Zn_2SiO_4:Mn (5 mol-%) and α-Zn_2SiO_4:Mn (5 mol-%) confirm this view (Fig. 7). Excitation spectra ($\lambda_{emission}$ = 579 nm and 529 nm) exhibit a characteristic intense and broad absorption between 250 and 320 nm. This is due to d-d transition on Mn^{2+} as the relevant luminescent center. All emission is driven by $^4T_1$ to $^6A_1$ relaxation on Mn^{2+}. The color of emission strongly depends on the relevant crystal field, and locally on the coordination and bond distances of the Mn^{2+} ion. To this concern, emission can vary in principle from green to red. More concrete, green emission is attributed to tetrahedrally coordinated Mn^{2+} and a comparably weak crystal field. In contrast, yellow to red emission is associated with octahedrally coordinated Mn^{2+} and a comparably strong crystal field. The observed emission of β-Zn_2SiO_4:Mn (550-610 nm) and α-Zn_2SiO_4:Mn (500-560 nm) is in accordance with the upper consideration and has been described for bulk materials in detail.[36]

Qualitatively, intense luminescence of nanoscale β-Zn_2SiO_4:Mn (5 mol-%) and α-Zn_2SiO_4:Mn (5 mol-%) can be visualized by UV-excitation (e.g. with a standard mercury discharge lamp) of powder samples as well as of dispersed particles (Fig. 7). Aiming at a quantification of the underlying luminescence, quantum yield is measured by comparison to a reference material that exhibits similar luminescent properties. Here, bulk Zn_2SiO_4:Mn (5 mol-%) - a standard phosphor for fluorescent lamps and plasma display panels - was applied. This reference consists of particles on a micron scale (4 to 8 µm in diameter) and is specified with a quantum yield of 80 %. As a result, quantum yields of 7 % for β-Zn_2SiO_4:Mn and 12 % for α-Zn_2SiO_4:Mn are obtained.

YVO_4:Eu@YF_3 core-shell nanoparticels

YVO_4:Eu nanocrystals were synthesized applying $[N(Me)(Bu)_3][N(Tf)_2]$ as ionic liquid as well as $YCl_3 \cdot 6H_2O$, $EuCl_3 \cdot 6H_2O$, and $VO(O^iPr)_3$ as starting materials. Previous studies - in contrast to bulk YVO_4:Eu typically doped with 5 mol-% - have evidenced an Eu^{3+} content of 15 mol-% to be most suited.[27,28] Consequently, this dopant level was applied here, too. For optimal conditions of particle nucleation the synthesis was performed at 50 °C in a mixture of IL and ethanol as a cosolvent. Role of the cosolvent, on the one hand, is to reduce the viscosity of the IL, and on the other hand, is to increase the solubility of the starting materials. Thereafter, ethanol was evaporated, and the pre-formed YVO_4:Eu nanoparticles were crystallized in the pure IL by heating to 200 °C. Finally, the as-prepared nanocrystals were washed to remove the IL and remaining salts (e.g. NaCl). YVO_4:Eu was obtained as a colorless powder that can be easily redispersed in polar solvents (e.g. water, methanol, ethanol, diethylene glycol) by sonification.

Composition, purity and crystallinity of as-prepared YVO_4:Eu nanoparticles are evidenced by X-ray powder diffraction. All Bragg peaks are in accordance to the tetragonal wakefieldite modification. The obvious broadening of the diffraction lines already hints to the presence of nanosized crystals. To this end, a mean crystallite size of 12 nm was calculated applying Scherrer's equation to the most intense Bragg peak ((200) at 2θ = 25.00°). Scanning electron microscopy (SEM) was involved to get a closer look at morphology and size (Fig. 8). The nanocrystals turn out to be non-agglomerated and very uniform in size and shape. The average diameter is deduced to 12-15 nm and consistent with the XRD results. In addition to XRD analysis, which confirms the crystallinity of powder samples, composition and crystallinity of selected individual nanoparticles are evidenced by high resolution transmission electron microscopy (HRTEM) and selected area electron diffraction (SAED) (Fig. 8). Representative images display YVO_4:Eu nanoparticles with highly ordered lattice fringes, indicating that even areas close to the particle surface are well crystallized. The observed lattice distance is identified as 6.22 Å and corresponds well with (001) (literature data: 6.27 Å).[29] During HRTEM investigation the nanocrystals turned out to become

amorphous on a minutes time scale (Fig. 8). In fact, such a behavior has been described already and is ascribed to phase separation processes and partial reduction of vanadium.[30]

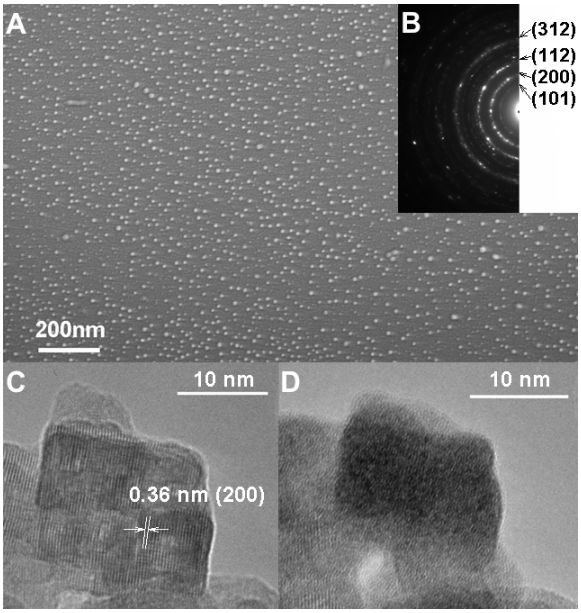

Figure 8. A) SEM, B) SAED, C) and D) HRTEM images of as-prepared YVO_4:Eu of a representative nanoparticle, thereof D) after about 1 min of electron-beam exposure.

In addition to electron microscopy, the particle size distribution of the title compound was measured in suspension via dynamic light scattering (DLS). To this concern, as-prepared YVO_4:Eu was redispersed in DEG. As a result, an average hydrodynamic diameter of 15 nm, and again a low degree of agglomeration is evidenced. The colloidal stability of the suspensions is ascribed to charge stabilization of the nanocrystals by the constituents of the IL.[31] Hence, infrared spectra of as-prepared YVO_4:Eu show the characteristic vibrations related to the $[VO_4]^{3-}$ anion as the dominating absorption ($\nu_{(V\text{-}O)}$ = 900-800 cm^{-1}). On the other hand, the IL ($\nu_{(C\text{-}H)}$ = 2970-2880 cm^{-1}, $\nu_{(S\text{-}O)}$ = 1470-1060 cm^{-1}) as well as water ($\nu_{(O\text{-}H)}$ = 3500-3300 cm^{-1}, $\delta_{(H2O)}$ = 1630 cm^{-1}) are indeed indicated by weak absorptions.[32]

Emission spectra of as-prepared YVO_4:Eu (15 mol-%) display the characteristic Eu^{3+}-related transitions as described for bulk as well as for nanoscale YVO_4:Eu. After excitation via (O→V) charge transfer on the vanadate anion and subsequent energy transfer to Eu^{3+}, relaxation occurs due to f-f transitions on Eu^{3+}, with $^5D_0 \rightarrow {}^7F_2$ as the most intense emission line.[33,34] The quantum yield was determined by comparison to commercial YVO_4:Eu, which is used as an industrial display phosphor. This reference material consists of particles, 4 to 8 µm in diameter and has been specified with a quantum yield of 70 %. Based on normalized absorption of sample and reference, by comparing the resulting emission intensity, a quantum yield of 17-19 % is obtained for as-prepared YVO_4:Eu nanocrystals. This value is in good agreement to literature data.

Aiming at an increased quantum yield - similar to semiconductor-type quantum dots - a core-shell structure would be most likely in order to decrease surface-related loss processes. In order to guarantee a sufficient lattice matching at the solid-solid interface, the non-luminescent shell is preferentially established by the same compound as the core - or at least a material with almost identical lattice parameters. Since $[VO_4]^{3-}$ as a luminescent center is an intrinsic part of the lattice, non-doped YVO_4 is excluded from being a suitable shell. Selection of a shell material is restricted even further due to the anisotropy of the YVO_4 unit cell. The situation is unraveled here by introducing YF_3 as a shell. In general, fluorides are well known for efficient defect healing of oxide materials.[35] Moreover, at least two lattice parameters of YVO_4 (a = b = 7.10 Å; c = 6.27 Å) are very

close to YF_3 (b = 6.85 Å; a = 6.35 Å).[36] HRTEM images indeed show a single crystalline YVO_4:Eu core, 12 to 15 nm in size, which is covered by a highly crystalline YF_3 shell, 1 to 2 nm in thickness (Fig. 9). The resulting core-shell particles amount to 14 to 17 nm in diameter and show a sufficient matching between (001) lattice fringes of YVO_4 (measured: 6.22 Å) and (100) fringes of YF_3 (measured: 6.39 Å). Although electron microscopy indicates the presence of a shell, these investigations are quite complicated due to the low stability of YVO_4 and its alteration when exposed to the electron beam. Standard analytical tools, e.g., DLS and XRD, are - as expected - of very limited reliability due to the low overall amount of YF_3. On the other hand, fluorescence spectroscopy is a very valuable evidence for the core-shell structure (see below). In addition, electron-energy loss spectroscopy (EELS) clearly validates the presence of fluorine throughout the sample (Fig. 10). Here, element mapping reveals high intensities of Eu in the inner parts of the nanoparticles, associated with low peripheral fluorine intensities. According to the Eu:F intensity ratio, the amount of fluorine can be deduced to about 1-3 %, which is in agreement to the expectation.

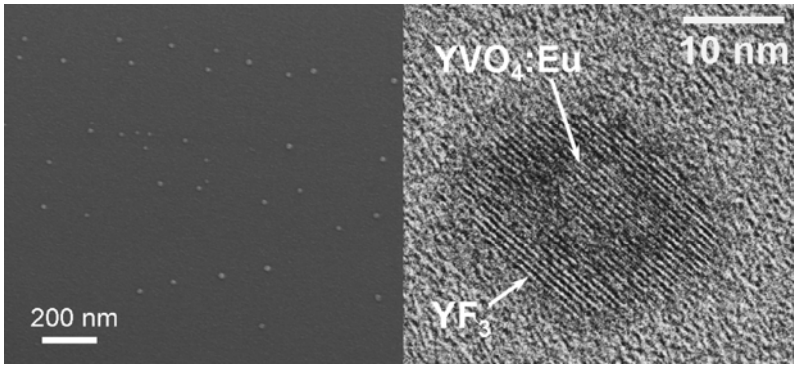

Figure 9. Overview SEM and HRTEM image of YVO_4:Eu@YF_3 core-shell nanoparticles, with YVO_4 core (001) = 6.22 Å and YF_3 shell (100) = 6.39 Å).

If core-shell structures are established with a sufficient lattice matching of core and shell, a significant increase in quantum yield can be expected.[35] Indeed, suspensions of YVO_4:Eu@YF_3 exhibit strong emission of red light even in ethanol. Emission spectra exhibit a strong increase in intensity when comparing YVO_4:Eu@YF_3 and YVO_4:Eu. Note that crystal field splitting of $^5D_0$-$^7F_2$ transitions results in a certain change of the emission ratio. The quantum yield of YVO_4:Eu@YF_3 (15 mol-%) was recorded again - as described above - by comparing to commercial YVO_4:Eu (5 mol-%) as a reference. As a result, a value of 44 to 46 % is obtained. Both results - the emission spectra as well as the quantum yield - are in accordance with a significant reduction of surface-allocated defects, and thereby confirm the presence of the core-shell structure.

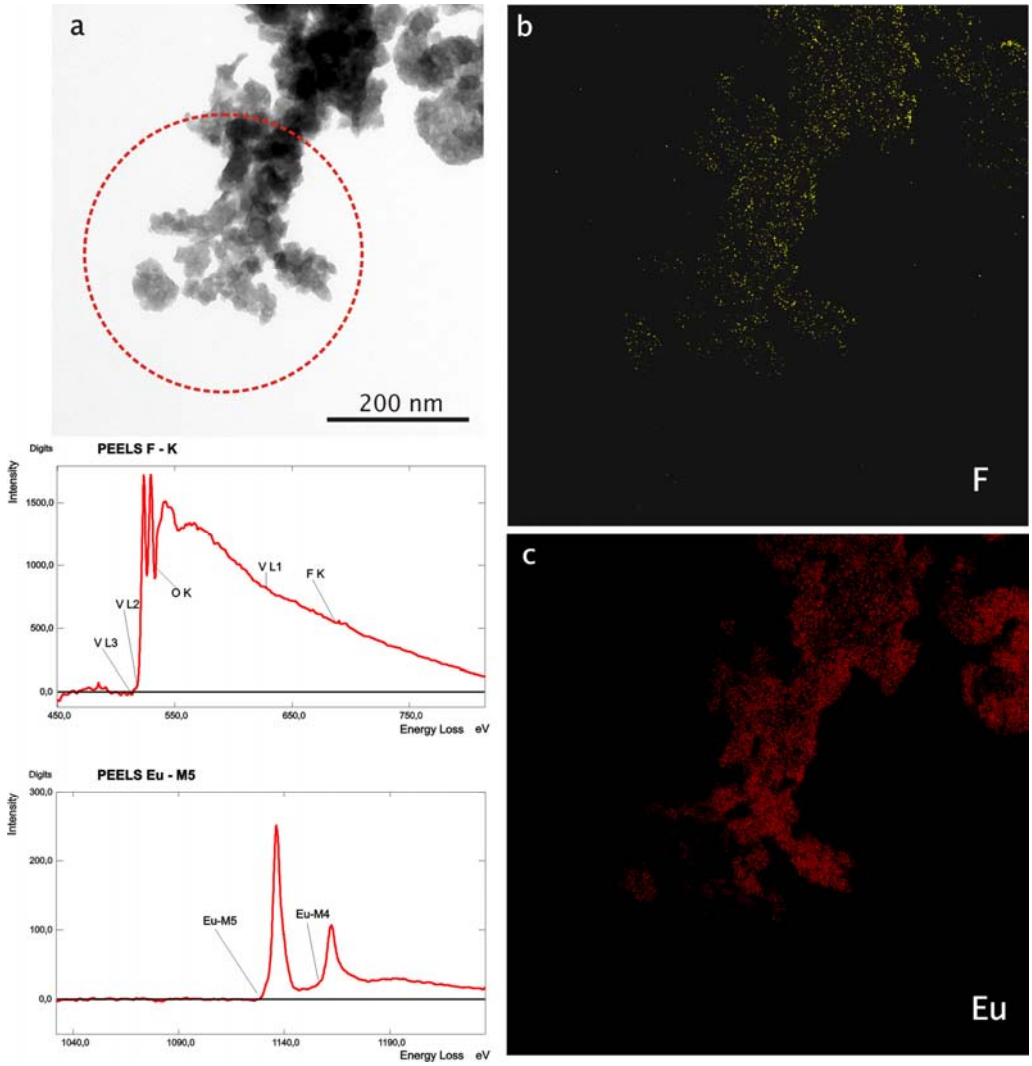

Figure 10. Electron-energy loss spectroscopy (EELS) of YVO_4:Eu@YF_3 colloid: (a) Bundles of nanoparticles adsorbed to a carbon-foil. Encircled area indicates the PEELS measuring area of the adjacent spectra, which were background corrected. (b, c) ESI-maps of F and Eu show their elemental distribution, strictly correlated with the particle bundles.

$In_2(MoO_4)_3$:Eu

$In_2(MoO_4)_3$ as a lattice material with quite a high reflectivity in the visible range could – upon selective doping – act as a luminescent nanomaterial. Thus, luminescence of rare earth ions driven by LMCT excitation and subsequent energy-transfer to the relevant rare-earth ion is well known for application in fluorescent lamps and displays. With regard to charge and size of In^{3+} (r: 94 pm) as the regular lattice constituent, Eu^{3+} (r: 108 pm) could be an ideal dopant. Accordingly, 5 mol-% Eu^{3+} were introduced in the lattice of as-prepared $In_2(MoO_4)_3$. The presence of Eu^{3+} becomes obvious already by comparing UV-Vis spectra of $In_2(MoO_4)_3$ and $In_2(MoO_4)_3$:Eu. Weak line-type absorptions between 350 nm and 600 nm originate from $^7F_0 \rightarrow {}^5D_n$ transitions on Eu^{3+}. Moreover, upon excitation with UV-light (366 nm) a weak red emission of $In_2(MoO_4)_3$:Eu is observed (Figure 11).

Excitation and emission spectra of as-prepared $In_2(MoO_4)_3$:Eu show the characteristic transitions within the 4f-manifold on Eu^{3+} as well as the $O^{2-} \rightarrow Eu^{3+}$ LMCT (Figure 12) as they are observed in many other Eu^{3+}-doped luminescent materials (e.g. Y_2O_3:Eu, YVO_4:Eu). Since the luminescence of nanomaterials is strongly affected by lattice defects, surface-allocated defect states or remaining

solvent adhered to the particle surface, as-prepared $In_2(MoO_4)_3$:Eu was heated for 30 min at 450 °C. By this measure, certain agglomeration of nanoparticles occurred, however, resuspension of the sintered material is still possible with an average primary diameter (51(11) nm) that is still near to the as-prepared material (35(6) nm) (Figure 10). The emission intensity, on the other hand, is dramatically increased subsequent to sintering. For suspensions as well as for powder samples this is clearly visible even with the naked eye (Figure 10). Since the Eu^{3+} concentration is identical for the as-prepared as well as for sintered $In_2(MoO_4)_3$:Eu, its excitation can be normalized based on the $^7F_0 \rightarrow {}^5D_n$ transitions. In concrete, the most intense excitation line at 394 nm was selected to this purpose. Thus, the emission can be compared quantitatively and results in a twelve-times higher emission of sintered $In_2(MoO_4)_3$:Eu.

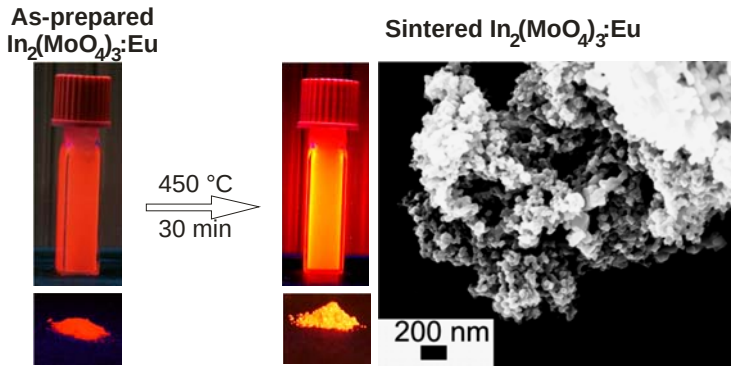

Figure 11. Visible emission ($\lambda_{excitation}$: 254 nm) of as-prepared $In_2(MoO_4)_3$:Eu (5 mol-%) as compared to the sintered material (450 °C, 30 min): powder samples and suspension in DEG as well as a SEM image of sintered $In_2(MoO_4)_3$:Eu.

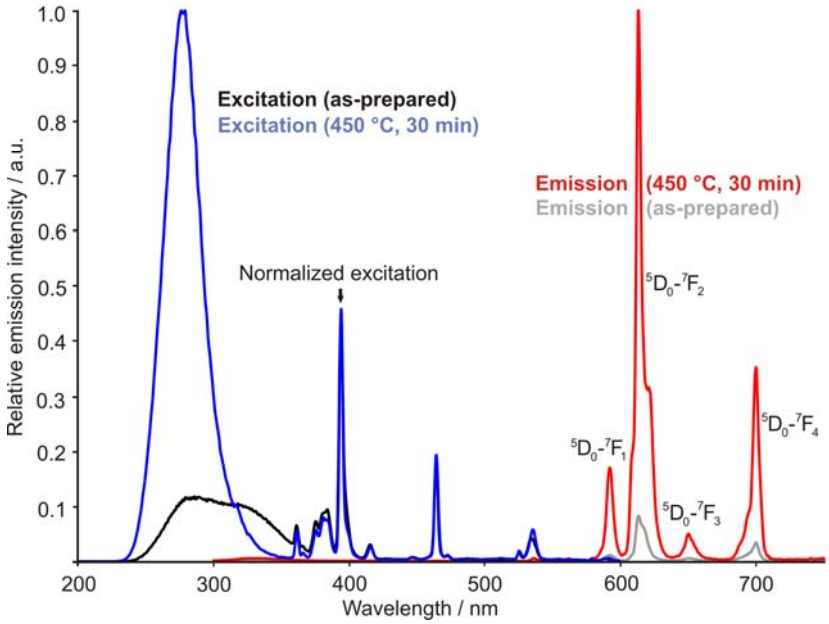

Figure 12. Excitation ($\lambda_{emission}$: 614 nm) and emission ($\lambda_{excitation}$: 250 nm) of as prepared $In_2(MoO_4)_3$:Eu (5 mol-%) as compared to the sintered material (450 °C, 30 min). Spectra were normalized on f→f excitation on Eu^{3+} at 394 nm.

2. Organic-inorganic hybrid luminescent nanomaterials

Imaging techniques (such as positron emission tomography, magnetic resonance tomography, X-ray tomography, luminescence imaging, optical coherence tomography, ultrasonic techniques) require new contrasting agents in humans, mice or rats to visualize whole organisms or single cells.[37] Moreover, new luminescent tags have to be developed for modern light microscopy. Subcellular-ultrastructural analysis with energy-filtered transmission electron microscopy (EFTEM), finally, requires electron-opaque markers for easy detection. To use custom-made nanoparticles as oligofunctional entities, various traits are prerequisite prior to a general application in life sciences and basic medical research, such as: (1) sufficient biocompatibility; (2) straightforward synthesis; (3) easy detection with standard hardware, and (4) highly specific signals to prevent overlaps with autofluorescence by organs, cells or organelles. Significant progress has been already made with regard to the above requirements and functions based on luminescent nanoparticles, and is summarized in some recent reviews.[38]

Three classes of luminescent nanoparticles have been identified at present: semiconductor-type quantum dots,[39] metal-doped oxides and fluorides,[40] and organic-inorganic hybrids.[41] Among them, quantum dots (e. g., CdSe@ZnS, InP@ZnS) are most prominent and widely applied, due to their intense emission, ranging from the blue to the infrared.[42] These materials, however, have inherent drawbacks, such as their sensitivity towards hydrolysis and oxidation, high demands on the crystallinity of the material, and very toxic constituents.[43] Advanced chemical synthesis and strategies for surface protection are prerequisites for obtaining state-of-the-art water-dispersible core-shell structures with precise size control.[44] The latter is essential to establish the underlying quantum size effect and a well-defined emission. Similar requirements − including the crystallinity of the material, core-shell structures and surface protection − also apply to metal-doped nanoparticles (e. g., $LaPO_4$:Ce,Tb@$LaPO_4$, LaF_3:Eu@LaF_3) to reduce surface-allocated defects and to obtain an intense emission.[45]

Hybrid materials, as an alternative class of luminescent nanoparticles, comprise a non-luminescent inorganic matrix (i. e., silica and calcium phosphate), in which a fluorescent organic dye (e. g. phenoxazine, Nile red, rhodamine, indocyanine green, fluorescein) is encapsulated.[46] With a dye concentration of 1 mol-% or less, the number of luminescent centers per particle is low, especially, in comparison to the quantum dots. Moreover, the available quantities are limited since these hybrid materials are commonly made via microemulsion techniques.

The aim of this study is to identify a low-cost biocompatible hybrid nanomaterial with intense luminescence. Chemical synthesis should be as easy as possible and potentially provide reliable access to larger quantities. The system $ZrO(HPO_4)_{1-x}(FMN)_x$ (x = 0 – 1) and its formal constituents $(ZrO)^{2+}$−$(HPO_4)^{2-}$−$(FMN)^{2-}$ (FMN: flavin mononucleotide − a derivative of the well-known vitamin B_2, Fig. 13)[47] attracted our attention for several reasons: 1.) The very low solubility, which facilitates nucleation and growth of nanoparticles;[48] 2.) The chemical inertness of zirconium phosphates; 3.) All constituents are known for their biocompatibility (e. g. lethal intake of $ZrCl_4$ >1 g/kg);[49] 4.) Depending on the chemical composition, the dye concentration can be tuned from very low contents (<1 mol%) up to molar amounts. The underlying concept of a luminescent hybrid material that is formally composed of an inorganic cation and an anionic fluorescent dye has not been reported previously.

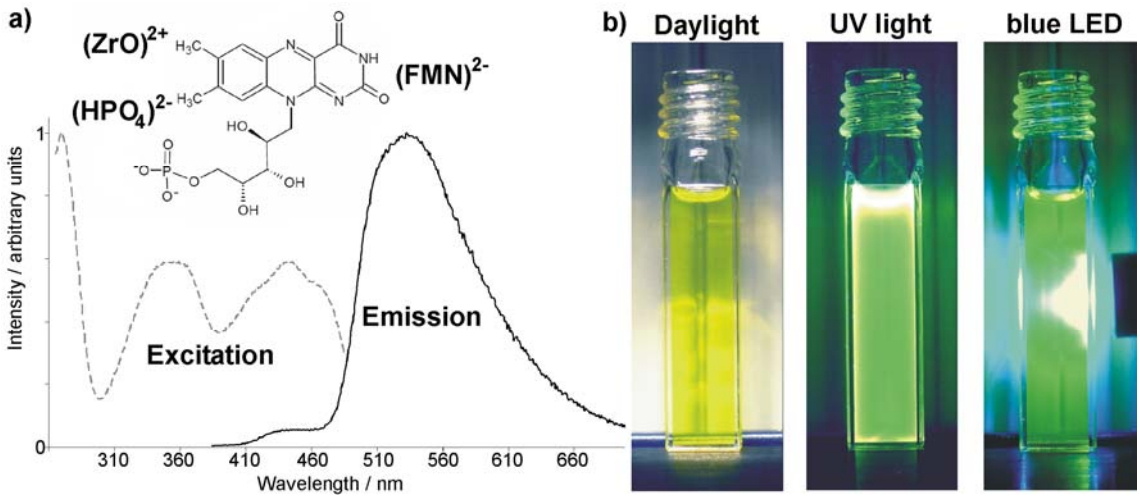

Figure 13. $ZrO(HPO_4)_{1-x}(FMN)_x$ (FMN: flavin mononucleotide) with: a) Its formal constitutents as well as excitation and emission spectra; b) Suspensions of as-prepared nanoparticles (1 wt-% in ethanol) in daylight, with UV excitation (366 nm) and with blue-LED excitation (380–450 nm).

The poor solubility of the zirconium phosphates, in principle, allows a preparation of nanoparticles via various methods. Aiming at a rapid synthesis that avoids advanced multistage procedures, we have decided to use a forced hydrolysis in water.[50] Based on a formula $ZrO(HPO_4)_{1-x}(FMN)_x$ (x = 0 – 1) a complete exchange of $(HPO_4)^{2-}$ and $(FMN)^{2-}$ should be possible, and is indeed observed for the first time with luminescent hybrid materials. To this end, the compound zirconyl flavin mononucleotide (ZrO(FMN)) containing molar amounts of the dye, and the "diluted" version $ZrO(HPO_4)_{0.9}(FMN)_{0.1}$ were selected as representative examples. Both compounds were obtained simply by mixing of aqueous solutions of the starting materials and resulted in transparent yellow to orange suspensions, which show bright green emission under ultraviolet (366 nm) as well as under blue light (380–450 nm) excitation (Fig. 13). Note that, due to the strong absorption of UV light, only that part of the suspension shows full luminescence which is close to the direction of incidence of the incoming light. In the case of the blue LED, partial additive color mixing of scattered blue light and the green emission is observed, leading to white light. As-prepared suspensions typically contain solid contents of 1 % by weight, and turn out to be stable over months. Although the synthesis was performed on the laboratory scale here (i. e. in 0.5–1.0 g amounts), straightforward scaling up can be expected due to the fact that, for instance, material's crystallinity or core-shell structures do not need any consideration.

Size and shape of as-prepared $ZrO(HPO_4)_{1-x}(FMN)_x$ were evaluated by dynamic light scattering (DLS), scanning electron microscopy (SEM), and transmission electron microscopy (TEM). DLS analysis of as-prepared nanoparticles in water shows a comparably broad size distribution with a mean hydrodynamic diameter of 39(±12) nm (Fig. 14). Redispersion in a more surface-active solvent such as diethylene glycol (DEG) leads to a much narrower size distribution (i. e. 32(±4) nm). This finding indicates that uniform primary particles are present in principle, but that a certain agglomeration in water occurs. Note that all particles are still smaller than 100 nm, even in water. Consider also the simplicity of the synthesis and the absence of any common colloidal stabilizer (e. g. long-chained amines or phosphines). By electron microscopy, $ZrO(HPO_4)_{1-x}(FMN)_x$ was observed with spherical shape and a mean diameter of 25–40 nm (Fig. 14). Finally, the specific surface was measured, based on the Brunauer-Emmett-Teller (BET) method. With a value of 115 m^2g^{-1}, the presence of a nanoscaled compound is again confirmed.

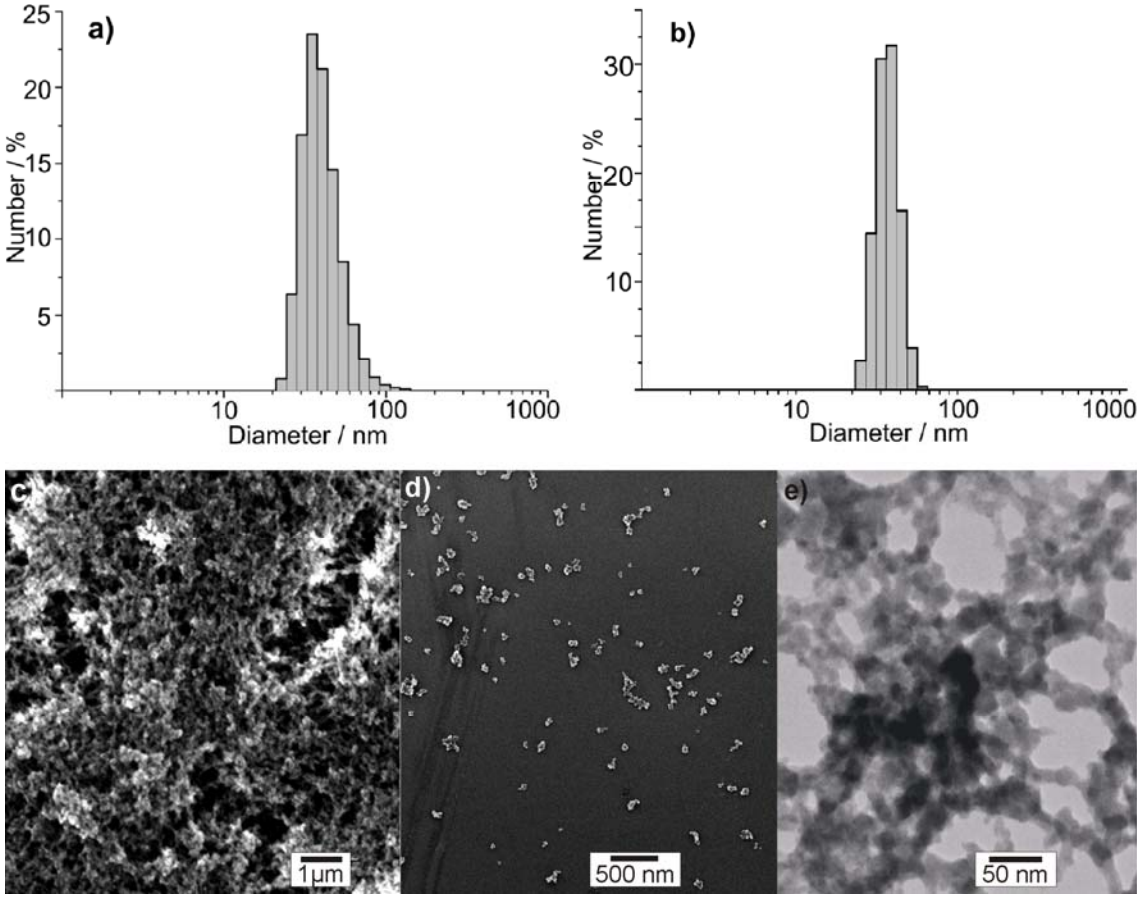

Figure 14. Size and morphology of $ZrO(HPO_4)_{1-x}(FMN)_x$: DLS analysis of as-prepared nanoparticles in water (a) and after redispersion in diethylene glycol (b); Electron microscopy of as-prepared nanoparticles at different magnification including overview SEM (c,d) and energy-filtered TEM zero-loss images (e).

To identify the chemical composition of the title compound, X-ray powder diffraction (XRD) analysis was conducted at first. However, the nanoparticles turned out to be completely amorphous. Fourier-transform infrared spectroscopy (FT-IR) evidences the presence and relative concentration of (FMN) by comparing $ZrO(HPO_4)_{0.9}(FMN)_{0.1}$ and ZrO(FMN) with $ZrO(HPO_4)$ and $Na(HFMN) \cdot 2H_2O$ as references (see supporting information). To investigate dye concentration and chemical composition, energy-dispersive X-ray absorption (EDX); elemental analysis and thermogravimetry (TG) were conducted as well. The Zr:P ratio of both compounds was determined by EDX and results to 1:1.2 for the composition $ZrO(HPO_4)_{0.9}(FMN)_{0.1}$ and to 1:1.0 for ZrO(FMN). Both values are well in agreement with the expected equimolar ratio. Elemental analysis (C/N analysis) of $ZrO(HPO_4)_{0.9}(FMN)_{0.1}$ and ZrO(FMN) revealed contents of 9.9 % carbon and 2.2 % nitrogen by weight (expected C: 8.5 %, N: 2.3 %) as well as 33.6 % carbon and 9.2 % nitrogen by weight (expected C: 36.3 %, N: 9.9 %), respectively. Finally, thermogravimetry of $ZrO(HPO_4)_{0.9}(FMN)_{0.1}$ showed a weight loss of 23 % when heated to 700 °C. This value − comprising the decomposition of the dye as well as the dehydration of the inorganic matrix − is in accordance with what has been expected (22 %). ZrO(FMN) showed a weight loss of 61 %, which can be directly correlated to the dye decomposition (expected: 64 %). The TG remnants of both compounds were identified via XRD, the results being $Zr_3(PO_4)_4$ and minor amounts of ZrO_2 (see supporting information).[51] Taking all these analytical data into account, the chemical composition of the amorphous nanoparticles can be reliably deduced to $ZrO(HPO_4)_{0.9}(FMN)_{0.1}$ and ZrO(FMN). Considering the enormous surface and the non-crystallinity of the nanoparticles, however, a certain protonation/hydration (e. g. $Zr(OH)_2(FMN)$) can not be excluded completely. Here, single-crystal

structure analysis would be most preferrable to explore the entire structure and bonding situation. Note that detailed structure and composition even of crystalline bulk zirconium phosphates are part of a controversial discussion so that conclusions by analogy are difficult, too.[51,52]

As expected, the photoluminescence of $ZrO(HPO_4)_{0.9}(FMN)_{0.1}$ and ZrO(FMN) is driven by the dye anion. Accordingly, the nanoparticles can be excited from the UV far into the visible spectrum (250−510 nm), accompanied by an intense emission with its maximum at 530 nm (Fig. 13).[48] Although FMN is very advantageous with regard to biocompatibility, its quantum yield (about 30 %)[48] is merely average by comparison to other fluorescent dyes. However, the nanoparticles − especially in the case of ZrO(FMN) − act as a quasi-infinite reservoir due to the incorporated molar amounts of the dye anion. This huge number of luminescent centers per nanoparticle guarantees an intensive spotlight-type emission as well as a low bleaching.

To evaluate the use of $ZrO(HPO_4)_{1-x}(FMN)_x$ nanoparticles for optical imaging techniques, we have concentrated our studies on living mice and cells. First, ZrO(FMN) was injected intradermally and intraperitoneally into NMRI (nu/nu) and BALB/C mice. An intense green emission was observed in the resulting wheals (Fig. 15a). The blood vessels around the wheals were detected after injection of Cy5-NHS, which reacted with intravascular blood proteins, blood cells and endothelial cells (Fig. 15b). The merged image (Fig. 15c) shows the borders of wheals with the vessels (red emission) especially after ethanol injection (ethanol induces hyperemia). The central part of the wheals instead shows intense green emission of the injected nanoparticles. The fluorescence of the ZrO(FMN) nanoparticles in wheals was stable for several hours and initially disappeared overnight. The intraperitoneal injection of 100−200 µl of nanoparticles in isotonic phosphate buffer, moreover, did not show any acute toxicity; even after two month, no toxic or allergic effects on the animals were observed.

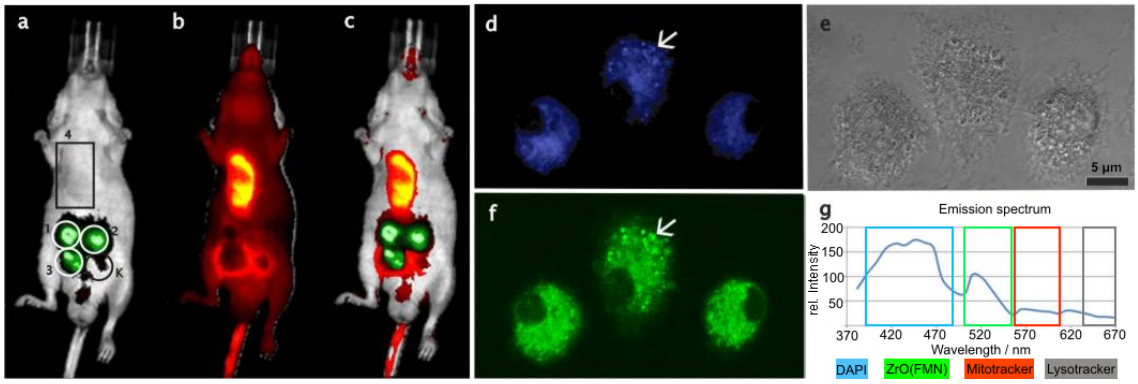

Figure 15. *In vivo* imaging of $ZrO(HPO_4)_{1-x}(FMN)_x$ nanoparticles in whole organisms and cells: a–c) Luminescence after intradermal injection into NMRI mice with a) ZrO(FMN) nanoparticles in (1) HEPES-buffer, (2) water, (3) ethanol as well as (4) Cy5-NHS intravescular vessel stain, (K) control buffer; b) Red fluorescence of Cy5-NHS; c) Merged images of (a+b); d–f) Cellular uptake of ZrO(FMN) in living murine macrophages with (d) vesicles and lysosomes stain by lysotracker; e) DIC image; f) Colocalization of vesicles with luminescent nanoparticles; g) Emission spectrum of four-color stain macrophages.

The biocompatibility of $ZrO(HPO_4)_{1-x}(FMN)_x$ nanoparticles was further investigated with mammalian cells, which respond to toxic substances and show a high uptake rate of nanoparticles (i. e., murine bone-marrow-derived macrophages, immature human dendritic cells). Both cell types took up the nanoparticles without showing any toxic effect, such as blebbing and cell death by apoptosis or necrosis. The nanoparticles colocalized with vesicles of the lysosomal compartment stained with lysotracker (Fig. 15d–f). They did not colocalize with mitochondria and nuclei. The

total emission spectrum measured over all stained cellular compartments confirmed the colocalization (Fig. 15g).

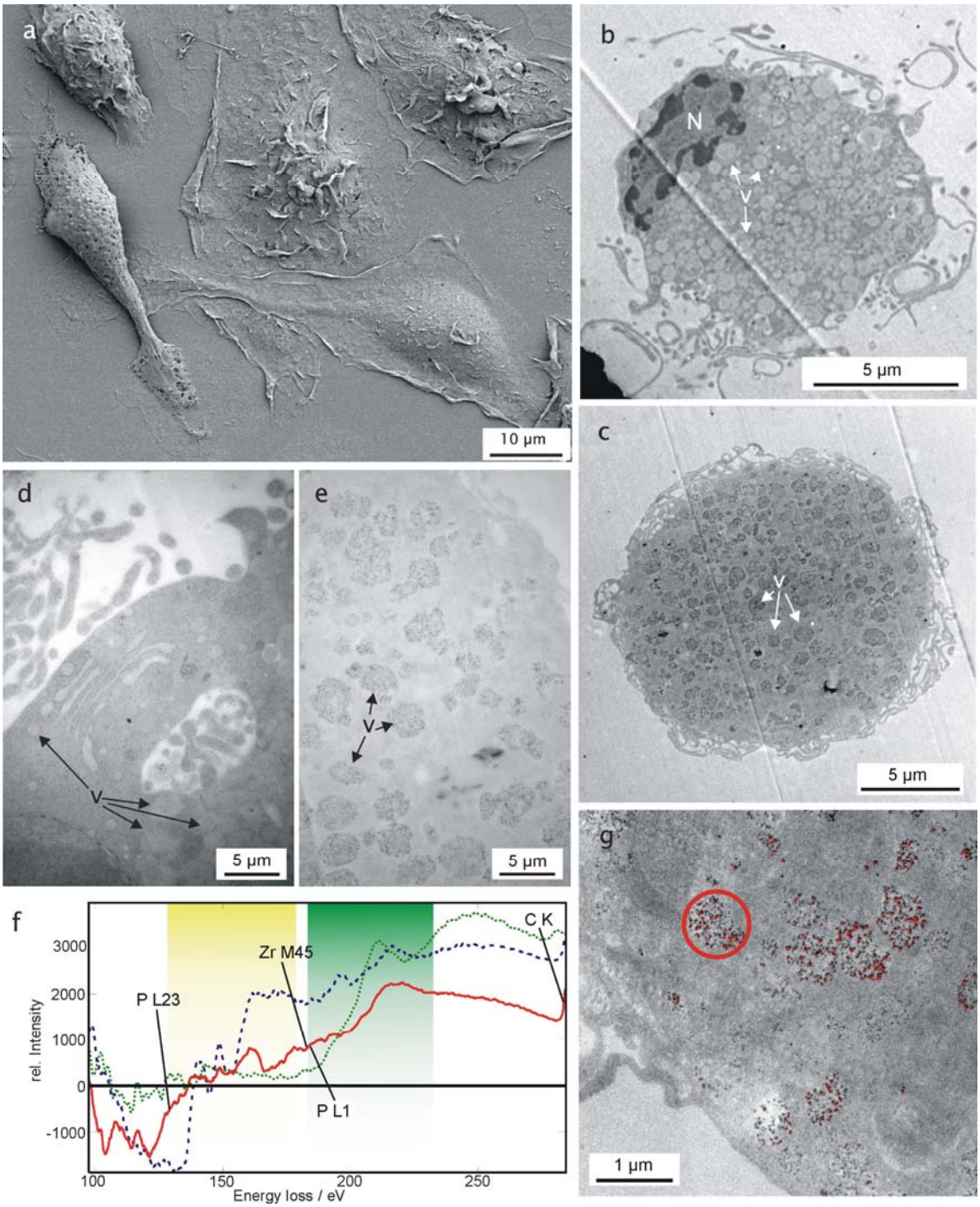

Figure 16. Ultrastructural and elemental analysis of $ZrO(HPO_4)_{1-x}(FMN)_x$-treated macrophages: a) Survey of confluently growing macrophages; b+d) Low-/high-resolution images of untreated macrophages (N: nucleus, V: cytoplasm with vesicles); c+e) Low-/high-resolution images of nanoparticle-treated macrophages; f) WR-PEEL spectra of: nanoparticle-filled vesicle (red line, measured vesicle indicated by red circle in (g)), ZrO(FMN) nanoparticles as such (blue line), elemental Zr as a reference (green line) as well as ionization onsets P–L23 (yellow box) and Zr–M45 (green box) with ELNES fingerprints; g) Vesicles overlaid with Zr–M45 elemental map indicating ZrO(FMN) nanoparticles as red dots.

SEM and EF-TEM verified the results of light microscopy and show the attached murine macrophages on plastic surface (Fig. 16a–e). The fixed macrophages were cut *"en face"* in parallel sections. In case of untreated macrophages nucleus and cytoplasm – crowded with electron-translucent vesicles – are clearly visible (Fig. 16b,d). In contrast, the cytoplasm of nanoparticle-treated macrophages is enriched with electron-opaque vesicles showing a characteristic dark, granular structure (Fig. 16c,e). Accordingly, the nanoparticles are exclusively localized in vesicles. Parallel electron-energy loss (PEEL) spectra of nanoparticle-containing vesicles and suited references (i. e., ZrO(FMN) as such, elemental Zirconium, ionization onsets of P–L23 and Zr–M45) evidence the presence of Zr and P in the nanoparticles (Fig. 16f). Macrophages incubated without nanoparticles do not show such structures (negative control). Finally, the ZrO(FMN) nanoparticles become precisely visible if the vesicles were overlaid with an Zr–M45 elemental map (Fig. 16f). Altogether, $ZrO(HPO_4)_{1-x}(FMN)_x$ nanoparticles appear to be suitable tools for staining viable structures in whole organisms. To establish a specific targeting in organisms, organs or cells − i. e., to couple specific antibodies, ligands, lectins or receptor molecules − all well-known techniques to functionalize the surface of semiconductor quantum dots and to attach specific linkers can now be applied.

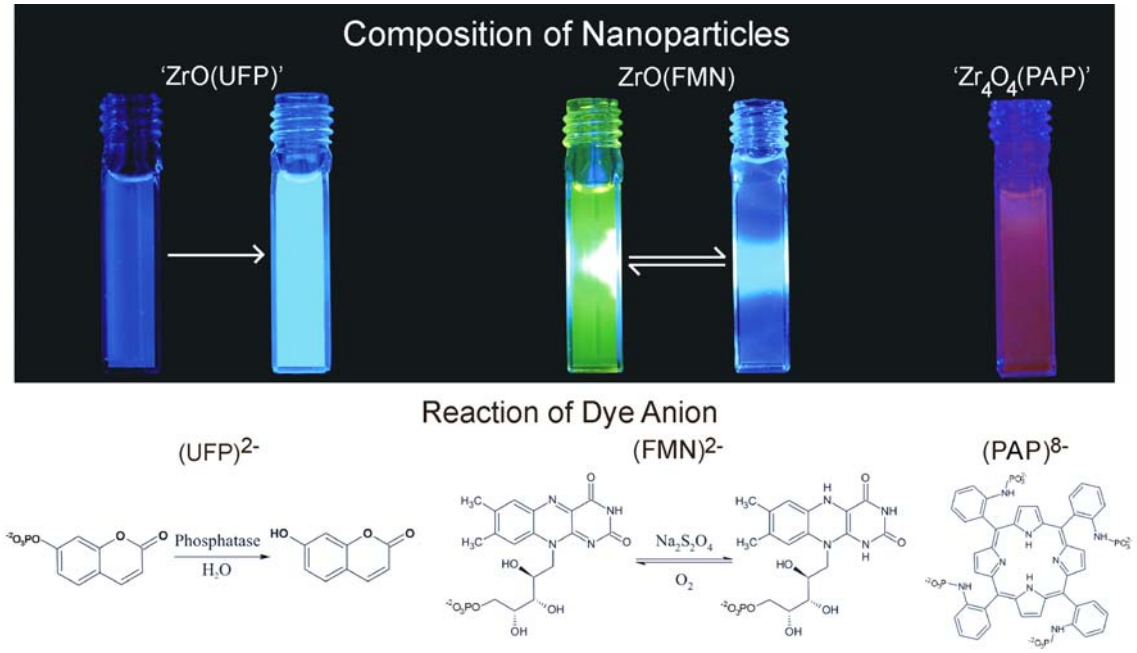

Figure 17. DMZP's with alternative emission color and luminescent switching: Combining the formal constituents $(ZrO)^{2+}$ and umbelliferonphosphate $(UFP)^{2-}$ or porphyrinamidophosphonate $(PAP)^{8-}$ as dye anions resulted in nanoparticles exhibiting blue and red emission ($\lambda_{excitation}$ = 366 nm). Luminescent switching is possible by addition of phosphatase in the case of "ZrO(UFP)" and by reduction/oxidation in the case of ZrO(FMN) (ZrO(FMN) excited with blue-LED).

In addition to $ZrO(HPO_4)_{1-x}(FMN)_x$ showing green emission, the concept of dye-modified zirconium phosphates (DMZP's) has been extended in a preliminary study to alternative dye anions and emission colors. When umbelliferon phosphate $(UFP)^{2-}$ was introduced, non-crystalline nanoparticles with an approximated composition "ZrO(UFP)" were obtained, exhibiting blue emission under 366 nm excitation (Fig. 17). In fact, emission is relatively weak here. A much brighter luminescence occurs if non-bound umbelliferon is set free in the presence of phosphatase. This change from weak to very strong emission can be of great relevance, since the effect can be directly correlated to metabolic activity, e. g. ATP consumption. A similar effect occurs in the case

of $ZrO(HPO_4)_{1-x}(FMN)_x$, whose emission can be turned on and off reversibly (Fig. 17). This is caused by reduction, such as in the presence of $[S_2O_4]^{2-}$, or oxidation, such as in the presence of O_2, of the dye, and might again allow a direct observation of metabolic processes (e. g. in the presence of NADH or NAD^+). A correlation of metabolic processes and optical switching of luminescent markers very recently attracted great interest.[53] Finally, red emission of DMZP's has been observed under blue light excitation with porphyrinamidophosphonate $(PAP)^{8-}$ as the dye anion and an approximated composition "$Zr_4O_4(PAP)$" (Fig. 17). As presented in the case of $ZrO(HPO_4)_{1-x}(FMN)_x$, "ZrO(UFP)" and "$Zr_4O_4(PAP)$" require a much more detailed elaboration regarding structure and properties as part of future studies. Nevertheless, both compounds demonstrate the practicability of DMZP's as a novel class of luminescent nanoparticles on a broader scope.

ZrO(UFP)

The organic-inorganic hybrid material ZrO(UFP) is accessible via synthesis in ionic liquids, namely $[MeBu_3N][NTf_2]$ (Me: methyl, Bu: Butyl, Tf: triflate). Such ionic liquids have been already used for the synthesis of various nanomaterials. In particular, they are beneficial because of their distinctive properties such as chemical and thermal stability, low surface tension and high polarity. Moreover, the constituting cations/anions are often weakly coordinating and therefore easy to remove from the particle surfaces subsequent to synthesis. All these aspects are relevant to the synthesis of nanoparticles, which was carried out in the case of ZrO(UFP) by mixing of the starting materials Na_2(UFP) and $ZrOCl_2$ at 70 °C in the ionic liquid as reaction medium. ZrO(UFP) herein is obtained as an insoluble colorless compound.

After separation from the ionic liquid and suited washing processes, as-prepared ZrO(UFP) can be easily resuspended in alcoholic media or water, typically with solid contents of 0.5−5.0 wt-%. Dynamic light scattering (DLS) of the resulting suspension − for instance in diethylene glycol (DEG) − results in a narrow size distribution with a mean diameter of 63(5) nm. Since water is the preferrable dispersant for all kinds of technical and biomedical applications, as-prepared ZrO(UFP) was resuspended in water, too. Here, DLS shows a broadened size distribution with a mean hydrodynamic diameter of 70(10) nm. Since water is less surface-active, this finding can be ascribed to a reduced colloidal stabilization of the nanoparticles and a beginning agglomeration. Scanning electron microscopy (SEM) confirms this view with a mean diameter of 47(9) nm. This value was deduced based on a statistical evaluation of 50 particles and is in reasonable agreement with the primary particle size as obtained by DLS for suspensions of ZrO(UFP) in DEG.

To identify the chemical composition of the as-prepared nanoparticles, X-ray powder diffraction analysis (XRD) was conducted first. However, the nanoparticles turned out to be completely amorphous. In order to validate the chemical composition of the compound, therefore, infrared spectroscopy (FT-IR), thermogravimetry (TG), energy dispersive X-ray analysis (EDX) and elemental analysis were involved. FT-IR spectra of the nanoparticles show all characteristic vibrational bands of umbelliferonephosphate: 3600–3000 cm^{-1} (ν(O–H)), 1750–1550 cm^{-1} (ν(C=O)), 1550–1200 cm^{-1} (ν(C–O), ν(C–C), δ(C–H)), 1200–900 cm^{-1} (ν(PO_4)) and 900–400 cm^{-1} (δ(C–C)). To allow for an easy assignment, the spectrum of Na_2(UFP) is displayed as a reference, too. Note that the large number of (energetically slightly different) phosphate ions in the amorphous nanomaterial results in a significant broadening of ν(PO_4) as compared to crystalline bulk-Na_2(UFP). In addition to the vibrations stemming from UFP, water as well as ethanol adhered to the surface of the nanoparticles are visible: 3600–3000 cm^{-1} (ν(O–H)) and 2950–2800 cm^{-1} (ν(C–H)). TG analysis of ZrO(UFP) showed reproducible weight losses of 32−39 % up to 500 °C. Hereof, a first step up to 250 °C can be attributed to decarboxylation (8 %). A second step is related to the complete fragmentation of the organic dye (29 %). These values are in accordance to the

expectation (12 % + 31 %). The TG remnant upon X-ray powder diffraction was identified as $Zr_3(PO_4)_4$ and minor amounts of ZrO_2.

While FT-IR spectroscopy and TG analysis prove the presence of the organic dye as well as of zirconium in principle, chemical analysis is required for quantification. Thus, EDX of the as-prepared nanoparticles revealed a composition of about Zr+Hf: 25+1(2) wt-%, P: 8(1) wt-%, C: 35(4) wt-%, O: 31(3) wt-%. These findings are in sufficient agreement with the calculated values for ZrO(UFP) with Zr: 26 wt-%, P: 9 wt-%, C: 31 wt-%, O: 32 wt-%. Note that commercially available Zirconium compounds always contain a certian amount of Hafnium (typically 1−3 % of the Zirconium concentration). Note further that the Zr:P ratio as the most significant result of the EDX analysis with Zr:P = 1.1:1.0 almost exactly amounts to the expected molar ratio (1:1). Taking all the above analytical data into account, the chemical composition of the amorphous nanoparticles is sufficiently curtailed to ZrO(UFP). Considering the large surface and the non-crystallinity of the nanoparticles, however, a certain protonation/hydration (e. g. $Zr(OH)_2$(UFP) as well as a certain incorporation of hydrogenphosphate instead of umbelliferonephosphate cannot be excluded completely. Since layer-type crystal structures have been quite often observed for hybrid-type zirconium compounds, a layered structure can be expected here, too. However, crystal growth and structural characterization of such compounds even in the ternary Zr-P-O system are known to be a challenge and have led to controversial discussions.

The photoluminescence of as-prepared ZrO(UFP) is measured with the nanoparticles suspended in water and compared to the non-bound fluorescent dye as a reference (Fig. 18). Accordingly, excitation and emission spectra of both are quite similar with the maxima at almost congruent positions, viz are 325 nm for excitation and 455 nm for emission. In fact, the quantum yield of umbelliferone with just 15 % is low in comparison to many other fluorescent dyes.[54-56] ZrO(UFP) nanoparticles nevertheless show an intense emission since the poor quantum yield is overcompensated by the huge number of luminescent centers per nanoparticle.

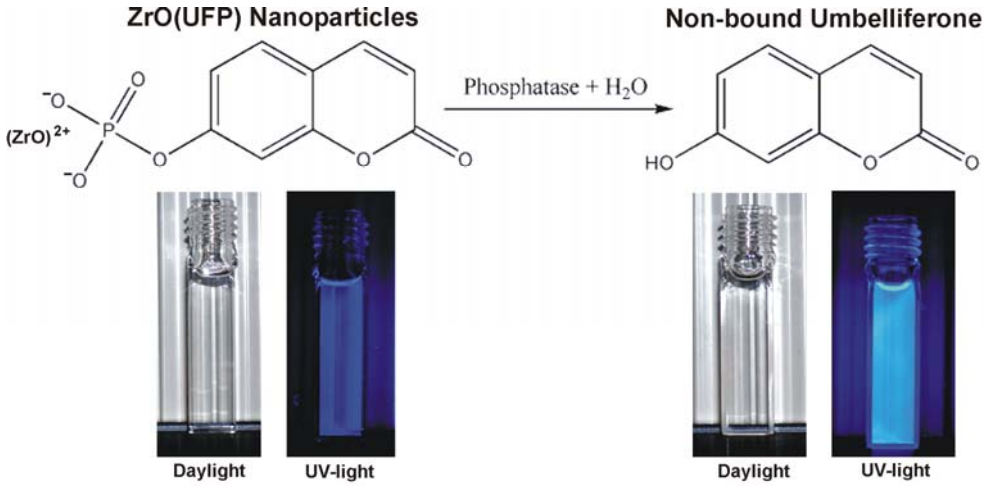

Figure 18: ZrO(UFP) nanoparticles in daylight and under UV-excitation indicating the appearance and luminescence of water-based suspensions prior (left cuevette each) and subsequent (right cuvettes each) to addition of acid phosphatase resulting in a controlled release of non-bound umbelliferone (suspensions in water; $\lambda_{excitation}$ = 366 nm).

Besides the UFP-related luminescence as-prepared ZrO(UFP) nanoparticles exhibit an additional dynamic emission process. Thus, a controlled release of umbelliferone from the nanoparticles can be initiated upon hydrolytic cleavage of the phosphate ester bond, for instance by addition of acid phosphatase. This release of free UFP leads to a significant increase of the emission intensity and is clearly visible even with the naked eye (Fig. 18). Comparing the luminescence of ZrO(UFP) nanoparticles before and after addition of acid phosphatase reliable evidences the effect of the

enzymatic reaction. The acid phosphatase driven hydrolytic release is further quantified by time-resolved photoluminescence spectroscopy (Fig. 19). To this concern, as-prepared ZrO(UFP) nanoparticles (suspended in 3 ml of H_2O) were measured first to guarantee for stable, continuous emission. Roughly after 4 h acid phosphatase enzyme was added (dissolved in 0.2 ml of H_2O). Addition of the enzyme solution is indicated by a dilution-caused drop in emission (Fig. 19). Thereafter the emission intensity rises within 10 h by a factor of 3–5.

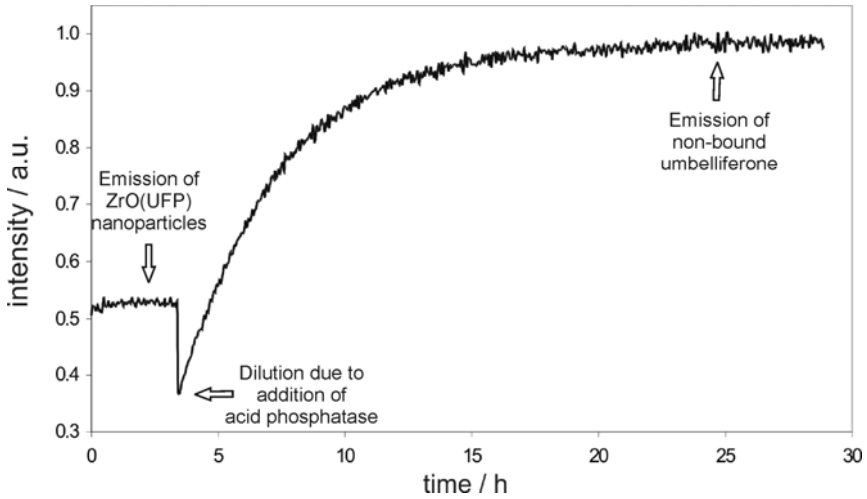

Figure 19: Increase of the luminescence intensity subsequent to phosphatase catalysed hydrolytic release of non-bound umbelliferone from ZrO(UFP) nanoparticles ($\lambda_{excitation}$ = 366 nm, $\lambda_{emission}$ = 456 nm).

Aiming at potential fields of application, umbelliferone and its derivatives generally play an essential role as secondary metabolites in several green plants, for instance, Typha domingensis, Apiaceae, Coronilla or Chamomilla recutita.[57-60] In opposite to the hepatotoxicity of some coumarine-like compounds, *7*-hydroxycoumarine and its derivates are known to be less harmful.[61] In fact, there are reports describing even a hepatoprotective and antiastmathic effect instead.[62-64] Umbelliferone is furthermore used as a pH-indicator, in sunblocking lotion and as a fluorescence indicator for analytical detection of Ca^{2+} or Cu^{2+}.[65] All these aspects may come into question for an application of ZrO(UFP) nanoparticles, too. In addition, ZrO(UFP) may act as a fluorescent probe for phosphatases or retarded carrier and release of umbelliferone as a pharmaceutical agent exhibiting hepatoprotective or antiastmathic effects.

References

- own work with complete titles -

[1] S. Shionoya, W. M. Yen (eds.), *Phosphor Handbook*, CRC Press, Boca Raton 1999.

[2] a) T. Pellegrino, S. Kudera, T. Liedl, A. M. Javier, L. Manna, W. Parak, *Small* **2005**, *1*, 48; b) C. Y. Zhang, H. C. Yeh, M. T. Kuroki, T. H. Wang, *Nature Materials* **2005**, *4*, 826; c) S. Kim, Y. T. Lim, E. G. Soltesz, A. M. DeGrand, J. Lee, A. Nakayama, J. A. Parker, T. Mihaljevic, R. G. Laurence, D. M. Dor, L. H. Cohn, M. G. Bawendi, J. V. Frangioni, *Nature Biotechnol.* **2003**, *22*, 93; d) B. Dubertret, P. Skourides, D. J. Norris, V. Noireaux, A. H. Brivanloue, A. Libchaber, *Sciene* **2002**, *298*, 1759; e) A. N. Shipway, E. Katz, I. Willner, *ChemPhysChem.* **2000**, *1*, 19;

[3] a) C. Feldmann, Polyol-mediated Synthesis of Nanoscale Functional Materials, *Adv. Funct. Mater.* **2003**, *13*, 101; b) S. T. Selvan, C. Bullen, M. Ashokkumar, P. Mulvaney, *Adv. Mater.* **2001**, *13*, 985; c) K. Riwotzki, H. Meyssamy, H. Schnablegger, A. Kornowski, M. Haase, *Angew. Chem.* **2001**, *113*, 574; *Angew. Chem. Int. Ed.* **2001**, *40*, 573; d) X. Peng, L. Manna, W. Yang, J. Wickham, E. Scher, A. Kadavanich, A. P. Alivisatos, *Nature* **2000**, *404*, 59; e) T. Vossmeyer, L. Katsikas, M. Giersig, I. G. Popov, K. Diesner, A. Chemseddine, A. Eychmüller, H. Weller, *J. Phys. Chem.* **1994**, *98*, 7665; f) C. B. Murray, D. J. Norris, M. G. Bawendi, *J. Am. Chem. Soc.* **1993**, *115*, 8706.

[4] a) J. S. Steckel, J. P. Zimmer, S. Coe-Sullivan, N. E. Scott, V. Bulovic, M. G. Bawendi, *Angew. Chem.* **2004**, *116*, 2206; *Angew. Chem. Int. Ed.* **2004**, *43*, 2154; b) J. W. Stouwdam, F. C. J. M. van Veggel, Langmuir **2004**, *20*, 11763; c) K. Kömpe, H. Borchert, J. Storz, A. Lobo, S. Adam, T. Möller, M. Haase, *Angew. Chem*. **2003**, *115*, 5672; *Angew. Chem. Int. Ed.* **2003**, *42*, 5513; d) M. T. Harrison, S. V. Kershaw, A. L. Rogach, A. Kornowski, A. Eychmüller, H. Weller, *Adv. Mater.* **2000**, *12*, 123.

[5] a) P. Wasserscheid, T. Welton (eds.), *Ionic Liquids in Synthesis*, Wiley-VCH, Weinheim 2002; b) W. Xu, C. A. Angeli, *Science* **2003**, *302*, 422; c) P. Bonhote, A. P. Dias, N. Papageorgiou, K. Kalyanasundaram, M. Grätzel, *Inorg. Chem.* **1996**, *35*, 1168.

[6] a) T. J. S. Schubert, *Nachr. Chem.* **2005**, *53*, 1222; b) J. Dupont, R. F. de Souza, P. A. Z. Suarez, *Chem. Rev.* **2002**, *102*, 3667; c) P. Wasserscheid, W. Keim, *Angew. Chem.* **2000**, *112*, 3926; *Angew. Chem. Int. Ed*. **2000**, *39*, 3772.

[7] a) B. Smarsly, H. Kaper, *Angew. Chem.* **2005**, *117*, 3876; *Angew. Chem. Int. Ed.* **2005**, *44*, 3809; b) M. Antonietti, D. Kuang, B. Smarsly, Y. Zhou, *Angew. Chem.* **2004**, *116*, 5096; *Angew. Chem. Int. Ed.* **2004**, *43*, 4989; c) H. Itoh, K. Naka, Y. Chujo, *J. Am. Chem. Soc*. **2004**, *126*, 3026; d) T. Nakashima, N. Kimizuka, *J. Am. Chem. Soc*. **2003**, *125*, 6386; e) G. S. Fonseca, A. P. Umpierre, P. F. P. Fichtner, S. R. Teixeira, J. Dupont, *Chem. Eur. J*. **2003**, *9*, 3263.

[8] I. Krossing, I. Raabe, *Angew. Chem.* **2004**, *116*, 2116; *Angew. Chem. Int. Ed.* **2004**, *43*, 2066.

[9] A. Tellenbach, C. Feldmann, unpublished results.

[10] D. F. Mullica, W. D. Milligan, D. A. Grossie, G. W. Beall, L. A. Boatner, *Inorg. Chem. Acta* **1984**, *95*, 231.

[11] J. Weidlein, U. Müller, K. Dehnike, *Schwingungsspektroskopie*, Thieme, Stuttgart 1988.

[12] G. Blasse, B. C. Grabmaier, *Luminescent Materials*, Springer, Berlin 1994.

[13] B. M. J. Smets, *Mater. Chem. Phys.* **1987**, *16*, 283.

[14] G. Bühler, C. Feldmann, patent application DE 10 2006 001 414.6.

[15] T. Welton, *Chem. Rev.* **1999**, *99*, 2071.

[16] S. Lebedkin, T. Langetepe, P. Sevillano, D. Fenske, M. M. Kappes, *J. Phys. Chem. B* **2002,** *106*, 9019.

[17] a) K. S. Mayya, F. Caruso, *Langmuir* **2003**, *19(17)*, 6987-6993; b) T. Nann, *J. Chem. Soc. Chem. Commun.* **2005**, *13*, 1735-1736; c) M. Sastry, *Current Sci.* **2003**, *85*, 1735-1745; d) D. I. Gittins, F. Caruso, *Angew. Chem*. **113** (2001) 3089-3092; *Angew. Chem. Int. Ed.* **2001**, *40*, 3001-3004.

[18] a) M. A. Aegerter, J. Puetz, G. Gasparro, N. Al-Dahoudi, *Optical Mater.* **2004**, *26*, 155-162; b) C. Meyer, M. Haase, Patent application WO 2004 096843 A1; c) G. Bühler, C. Feldmann, One-pot Synthesis and Application of Luminescent $LaPO_4$:RE (RE = Ce, Tb, Eu) Dispersions, *Appl. Phys. A* **2007**, *87***,** 631-636.

[19] a) H. Matsuno, T. Igarashi, T. Hiramoto, F. Takemoto, N. Hishinuma, Y. Oonishi, K Kasagi, T. Asahina, Y. Wakahata, Patent application EP 19950308; b) J. Y. Zhang, I. W. Boyd, *J. Appl. Phys.* **1998**, *84*, 1174-1178.

[20] K. Trampert, U. Lemmer, W. Heering, A. Zharkouskaya, C. Feldmann, Transparente Strahlungsquelle und Verfahren zur Strahlungserzeugung, *Patent application*, DE 10 2007 006 861.3.
[21] A. P. Abbott, G. Capper, D. L. Davies, R. K. Rasheed, V. Tambyrajah, *Green Chem.* **2002**, *4*, 24.
[22] I. W. Sun, S. Y. Wu, C. H. Su, Y. L. Shu, P. L. Wu, *J. Chin. Chem. Soc.* **2004**, *51*, 367.
[23] A. P. Abbott, T. J. Bell, S. Handa, B. Stoddart, *Green Chem.* **2005**, *7*, 705.
[24] D. P. Liu, G. D. Li, Y. Su, J. S. Chen, *Angew. Chem.* **2006**, *118*, 7530; *Angew. Chem. Int. Ed.* **2006**, *45*, 7370.
[25] C. Bull, G. F. J. Garlick, *J. Electrochem. Soc.* **1951**, *98*, 371.
[26] G. Blasse, C. Grabmaier, *Luminescent Materials*, Springer, Berlin, **1994**.
[27] Huignard A, Gacoin T, Boillot JP (2000) Chem. Mater. 12:1090.
[28] Blasse G, Bril A (1970) Philips Techn. Rev. 31:304.
[29] Milligan WO, Vernon LW (1952) J. Phys. Chem. 56:145.
[30] Hansen S, Smith DJ (1987) Electron Microsc. Anal. 151.
[31] [Antonietti M, Kuang D, Smarsly B, Zhou Y (2004) Angew. Chem. 117:5096; (2004) Angew. Chem. Int. Ed. 43:4989.
[32] Weidlein J, Müller U, Dehnike K Schwingungsspektroskopie, Thieme: Stuttgart 1988.
[33] Blasse, G.; Grabmaier BC Luminescent Materials, Springer: Berlin 1994.
[34] Brecher C, Samuleson H, Lempicki A, Riley R, Peters T (1967) Phys. Rev. 155:178.
[35] West AR Solid State Chemistry and its Applications, Wiley: Chichester 1990, pp. 318.
[36] Cheetham AK, Norman N (1974) Acta Chem. Scand. A 28:55.
[37] J. G. Fujimoto, D. Farkas, *Biomedical Optical Imaging*, Oxford University Press, Oxford 2009.
[38] a) H. Hang, D. Yee, C. Wang, *Nanomed.* **2008**, *3*, 83–91; b) R. C. Somers, M. G. Bawendi, D. G. Nocera, *Chem. Soc. Rev.* **2007**, *36*, 579–591; c) X. Michalet, F. F. Pinaud, L. A. Bentolila, J. M. Tsay, S. Doose, J. J. Li, G. Sundaresan, A. M. Wu, S. S. Gambhir, S. Weiss, *Science* **2005**, *307*, 538–544.
[39] a) B. Nitzsche, F. Ruhnow, S. Diez, *Nature Nanotechnol.* **2008**, *3*, 552–556; b) S. J. Clarke, C. A. Hollmann, Z. Zhang, D. Suffern, S. E. Bradforth, N. M. Dimitrijevic, W. G. Minarik, J. L. Nadeau, *Nature Mater.* **2006**, *5*, 409–417; c) M. K. So, C. Xu, A. M. Loening, S. S. Gambhir, J. Rao, *Nature Biotechnol.* **2006**, *24*, 339–343.
[40] X. F. Yu, L. D. Chen, M. Li, M. Y. Xie, L. Zhou, Y. Li, Q. Q. Wang, *Adv. Mater.* **2008**, *20*, 4118–4123.
[41] C. Sanchez, B. Lebeau, F. Chaput, J. P. Boilot, *Adv. Mater.* **2003**, *15*, 1969–1994.
[42] a) A. M. Smith, S. Dave, S. Nie, L. True, X. Gao, *Expert Rev. Mol. Diagn.* **2006**, *6*, 231–244; b) Z. Liu, A. Kumbhar, D. Xu, J. Zhang, Z. Sun, J. Fang, *Angew. Chem. Int. Ed.* **2008**, *47*, 3540–3542.
[43] a) Y. Su, Y. He, H. Lu, L. Sai, Q. Li, W. Li, L. Wang, P. Shen, Q. Huang, C. Fan, *Biomater.* **2008**, *30*, 19–25; b) J. Curtis, M. Greenberg, J. Kester, S. Phillips, G. Krieger, *Toxicol. Rev.* **2006**, *25*, 245–260.
[44] a) J. S. Steckel, J. P. Zimmer, S. Coe-Sullivan, N. E. Scott, V. Bulovic, M. G. Bawendi, *Angew. Chem. Int. Ed.* **2004**, *43*, 2154–2158; b) X. L. Peng, L. Manna, W. Yang, J. Wickham, E. Scher, A. Kadavanich, A. P. Alivisatos, *Nature* **2000**, *404*, 59–61.
[45] a) F. Meiser, C. Cortez, F. Caruso, *Angew. Chem. Int. Ed.* **2004**, *43*, 5954–5957; b) J. W. Stouwdam, F. C. J. M. van Veggel, *Langmuir* **2004**, *20*, 11763–11771.
[46] a) I. Sokolov, S. Naik, *Small* **2008**, *4*, 934–939; b) T. T. Morgan, H. S. Muddana, E. I. Altinoglu, S. M. Rouse, T. Tabakivic, T. Tabouillot, T. J. Russin, S. S. Shanmugavelandy, P. J. Butler, P. C. Eklund, J. K. Yun, M. Kester, J. H. Adair, *Nano Lett.* **2008**, *8*, 4108–4115; c)

H. Ow, D. R. Larson, M. Srivastava, B. A. Baird, W. W. Webb, U. Wiesner, *Nano Lett.* **2005**, *5*, 113–117.
[47] H. Du, R. A. Fuh, J. Li, A. Corkan, J. S. Lindsey, *Photochem. Photobiol.* **1998**, *68*, 141–142.
[48] A. Clearfield, R. H. Blessing, J. A. Stynes, *J. Inorg. Nucl. Chem.* **1968**, *30,* 2249–2258.
[49] S. Gosh, A. Sharma, G. Talukder, *Biol. Trace Element Res.* **1992**, *35*, 247–271.
[50] E. Matijevic, *Chem. Mater.* **1993**, *5*, 412–426.
[51] a) J. M. Troup, A. Clearfield, *Inorg. Chem.* **1977**, *16*, 3311–3314; b) J. Alamo, R. Roy, *J. Am. Ceram. Soc.* **1984**, *67*, C80–C82; c) V. I. Petkov, E. A. Asabina, K. V. Kiryanov, A. V. Markin, N. N. Smirnova, D. B. Kitaev, A. M. Kovalsky, *J. Chem. Thermodyn.* **2005**, *37*, 467–476; d) A. Orlova, S. G. Samoilov, G. N. Kazantsev, V. Y. Volgutov, D. M. Bykov, A. V. Golubev, E. Y. Borovikova, *Crystallogr. Rep.* **2009**, *54*, 431–438.
[52] a) P. H. Mutin, G. Guerrero, A. Viaux, *C. R. Chim.* **2003**, *6*, 1153–1164; b) E. Brunet, M. Alonso, C. Cerro, O. Juanes, J. C. Rodriguez-Ubis, Á. E. Kaifer, *Adv. Funct. Mater.* **2007**, *17*, 1603–1610.
[53] a) D. Lee, S. Khaja, J. C. Velasquez-Castano, M. Dasari, C. Sun, J. Petros, W. R. Taylor, N. Murthy, *Nature Mater.* **2007**, *6*, 765–769; b) M. Andresen, A. C. Stiel, J. Folling, D. Wenzel, A. Schonle, A. Egner, C. Eggeling, S. W. Hell, S. Jakobs, *Nature Biotechnol.* **2008**, *26*, 1035–1040; c) W. Wu, A. D. Q. Li, *Nanomed.* **2007**, *2*, 523–531.
[54] A. Orlova, S. G. Samoilov, G. N. Kazantsev, V. Y. Volgutov, D. M. Bykov, A. V. Golubev, E. Y. Borovikova, *Crystallogr. Rep.* **2009**, *54*, 431.
[55] J. R. Heldt, J. Heldt, S. Marek, H. A. Diehl, *Spectrochim. Acta A* **1995**, *51*, 1549.
[56] H. Czili, A. Horváth, *Appl. Catal. B.* **2008**, *81*, 295.
[57] G. G. Guilbault, S. H. Sadar, R. Glazer, J. Haynes, *Anal. Lett.* **1968**, *1*, 333.
[58] J. F. Vasconcelos, M. M. Teixeira, J. M. Barbosa-Filho, M. F. Agra, X. P. Nunes, A. M. Giulietti, R. Ribeiro-dos-Santos, M. B. P. Soares, *Eur. J. Pharmacol.* **2009**, *609*, 126.
[59] V. Stanjek, J. Piel, W. Boland, *Phytochem.* **1999**, *50*, 1141.
[60] V. N. Kovalev, A. N. Komissarenko, *Khimiya Prirodnykh Soedinenii* **1984**, *2*, 246.
[61] M. Repčák, J. Imrich, M. Franeková, *J. Plant. Physiol.* **2001**, *158*, 1085.
[62] D. Loew, H. Hauer, E. Koch, *Pharm. Zeit.* **2009**, *7*, 154.
[63] B. Ramesh, K. V. Pugalendi, *Indian J. Pharmacol.* **2006**, *38*, 209.
[64] B. Ramesh, P. Viswanathan, K. V. Pugalendi, *Eur. J. Pharmacol.* **2007**, *566*, 231.
[65] J. F. Vasconcelos, M. M. Teixeira, J. M. Barbosa-Filho, M. F. Agra, X. P. Nunes, A. M. Giulietti, R. Ribeiro-dos-Santos, M.B.P. Soares, *Eur. J. Pharmacol.* **2009**, *609*, 126.
[66] Römpp Chemielexikon online, *Thieme Medical*, Stuttgart 2009.